THE JOURNAL OF PHYSICAL CHEMISTRY A

Article

pubs.acs.org/JPCA

# Determination of the Rate Constant for the OH($X^2\Pi$) + OH($X^2\Pi$) → $H_2O$ + O($^3P$) Reaction Over the Temperature Range 295 to 701 K

Gokhan Altinay and R. Glen Macdonald*

Chemical Sciences and Engineering Division, Argonne National Laboratory, 9700 South Cass Avenue, Argonne, Illinois 60439-4381, United States

**ABSTRACT:** The rate constant for the radical−radical reaction OH($X^2\Pi$) + OH($X^2\Pi$) → $H_2O$ + O($^3P$) has been measured over the temperature and pressure ranges 295−701 K and 2−12 Torr, respectively, in mixtures of $CF_4$, $N_2O$, and $H_2O$. The OH radical was produced by the 193 nm laser photolysis of $N_2O$. The resulting O($^1D$) atoms reacted rapidly with $H_2O$ to produce the OH radical. The OH radical was detected by high-resolution time-resolved infrared absorption spectroscopy using a single Λ-doublet component of the OH(1,0) $P_{1e/f}(4.5)$ fundamental vibrational transition. A detailed kinetic model was used to determine the reaction rate constant as a function of temperature. These experiments were conducted in a new temperature controlled reaction chamber. The values of the measured rate constants are quite similar to the previous measurements from this laboratory of Bahng and Macdonald (*J. Phys. Chem. A* **2007**, *111*, 3850−3861); however, they cover a much larger temperature range. The results of the present work do not agree with recent measurements of Sangwan and Krasnoperov (*J. Phys. Chem. A* **2012**, *116*, 11817−11822). At 295 K the rate constant of the title reaction was found to be $(2.52 \pm 0.63) \times 10^{-12}$ cm$^3$ molecule$^{-1}$ s$^{-1}$, where the uncertainty includes both experimental scatter and an estimate of systematic errors at the 95% confidence limit. Over the temperature range of the experiments, the rate constant can be represented by $k_{1a} = 4.79 \times 10^{-18} T^{1.79} \exp(879.0/T)$ cm$^3$ molecule$^{-1}$ s$^{-1}$ with a uncertainty of ±24% at the 2$\sigma$ level, including experimental scatter and systematic error.

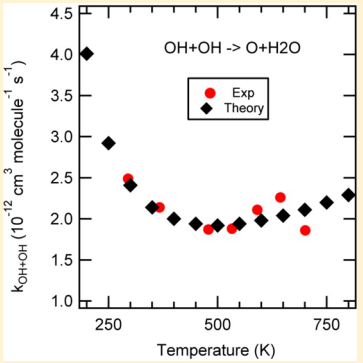


## I. INTRODUCTION

The OH radical plays an important role in both combustion and atmospheric chemistry. As such, its chemistry has been widely studied and characterized especially for bimolecular reactions involving hydrogen containing molecules. On the other hand, reactions of the OH radical with other transient species have received much less attention but can have important implications for combustion chemistry under high-pressure conditions.[1] The self-reaction of OH radicals is one of the most important examples of these reactions. The reaction proceeds by two channels:

$$OH(^2\Pi) + OH(^2\Pi) \rightarrow O(^3P) + H_2O \quad (1a)$$

$$OH(^2\Pi) + OH(^2\Pi) + M \rightarrow H_2O_2 + M \quad (1b)$$

In combustion chemistry, reaction 1a is chain propagating and 1b is chain terminating whereas the reverse of each of these channels also plays an important role because they are chain branching steps. For this reason, the study of reaction 1 in a more easily accessible temperature range also provides information on these reverse channels as well. The abstraction channel, reaction 1a, is pressure independent and proceeds on the lowest two energetically accessible triplet potential energy surfaces (PESs), $1^3A''$ and $2^3A'$. On the other hand, reaction 1b is pressure dependent and proceeds on the lowest energetically accessible singlet surface of electronic symmetry $1^1A'$. The OH($^2\Pi$) radical possesses both electronic and spin angular momentum producing 2($^1A'$ and $^1A''$) and 2($^3A''$ and $^3A'$) in the interaction of two OH radicals. Thus, not only is reaction 1 an important combustion and atmospheric reaction but it also offers a unique opportunity to investigate the role multiple PESs can play in a chemical interaction.[2]

Reaction 1a is considered prototypical of a radical−radical reaction, and there have been numerous experimental and theoretical studies to determine its rate constant. Most of the experimental measurements[3−14] have been conducted near 300 K using a variety of techniques to monitor the OH radical and determine its concentration. Two recent works[12,13] have reviewed this literature and will not be repeated here. Bahng and Macdonald[12] used the same laser flash photolysis technique as in the present work to generate the OH radical but monitored the temporal dependence of OH by high-resolution time-resolved absorption spectroscopy using a single Λ-doublet component of the OH(2,0) $P_{1e/1f}(4.5)$ first overtone transition. This detection method provides a direct measurement of the OH concentration. These experiments were conducted over a limited temperature range of 293−373 K and at low pressures of 2.6−7.8 Torr, to minimize contributions to OH removal by reaction 1b. At 293 K, these workers found $k_{1a}$ to be $(2.7 \pm 0.9) \times 10^{-12}$ cm$^3$ molecule$^{-1}$ s$^{-1}$, where the error bars include both scatter and systematic uncertainty at the 2$\sigma$ level, with $k_{1a}$ decreasing slightly with increasing temperature. The rate constants for reaction 1a measured by Bahng and Macdonald

**Received:** September 18, 2013
**Revised:** December 11, 2013
**Published:** December 13, 2013

 © 2013 American Chemical Society  dx.doi.org/10.1021/jp409344q | *J. Phys. Chem. A* 2014, 118, 38−54

were almost a factor of 2 larger than the IUPAC recommendation. Sangwan et al.[13] measured both the $k_{1a}$ and $k_{1b}$ over an extended temperature range 298−834 K and pressure range of 1−100 bar in a He bath gas. These workers also used 193 nm laser flash photolysis of $N_2O$ to generate OH radicals but monitored the OH temporal concentration profiles using a continuous UV OH resonance lamp. The OH concentration was quantified using accurate in situ actinometry. The number of independent kinetic parameters was too large to fit their OH profiles without restrictions. They adopted the IUPAC recommendation for $k_{1a}$ at low temperature and the recommendations of Troe[15] for the temperature dependence of the high-pressure limiting rate constant, $k_\infty$, and the broadening parameter, $F_c$. At temperatures above 414 K, they were able to determine $k_{1a}$ over the temperature range 555−834 K. With these restrictions, they determined both the high-pressure and low-pressure limiting rate constants at 300 K; however, both these limiting rate constants were found to be substantially different from the recommendations of Troe[15] and the detailed theoretical treatment of Selleevåg et al.[16] Recently, Sangwan and Krasnoperov[14] measured $k_{1a}$ over the temperature range 295−414 K. These workers used the recombination reaction O + $O_2$ + M → $O_3$ + M at pressures of 3 and 10 bar to followed the O($^3$P) atom production from reaction 1a by monitoring the appearance of $O_3$ using UV absorption spectroscopy. This is not a direct measurement of $k_{1a}$ but relies on the known rate constant data on the system to provide an accurate account of the chemistry at primarily 10 bar pressure. At 295 K, Sangwan and Krasnoperov found $k_{1a}$ to be $(1.40 \pm 0.46) \times 10^{-12}$ cm$^3$ molecule$^{-1}$ s$^{-1}$, where the error bars are the scatter in the data at the 2$\sigma$ level, decreasing slightly with increasing temperature. Their results were in excellent agreement with the IUPAC recommendation, largely determined by the discharge/flow, mass spectrometry measurements by Bedjanian et al.[10] and the discharge/flow, mass spectrometry, resonance fluorescence measurements of Sun and Li.[11] The current work is an extension of the previous work from this laboratory[12] on reaction 1a using a fundamental OH($v$ = 1,0) vibrational transition to monitor OH and an increased temperature range for the rate constant measurements.

The first serious attempt to provide a theoretical description of reaction 1a was by Harding and Wagner.[17] These workers used ab initio methods to describe the transition state regions for the two lowest triplet states, $1^3A''$ and $2^3A'$ using two electronic structure methods, MCSCF and GVB+1+2, both using polarized double-$\zeta$ basis sets. The barrier heights were scaled to describe the 300 K rate constant data at that time. The rate constants were calculated using variational transition state theory. The theory described the available experimental rate constant data from 300 to 2000 K. These workers pointed out two notable effects, at low temperatures tunneling accounted for a large fraction of the reactive flux and at higher temperatures the $2^3A'$ PES made an increasing larger contribution to the reactive flux. Recently, Nguyen and Stanton[18] have reported on an extended ab initio study of reaction 1a using the accurate HEAT-345(Q) protocol,[19] which treats electron correlation up to quadruple excitations. The rate constants for reaction 1a were calculated using semiclassical transition state theory and included an accurate description of quantum mechanical tunneling. As will be seen, the theoretical calculations for $k_{1a}$ are in excellent agreement with those of this work from 295 to 701 K and high-temperature shock tube data.[20−22] Nguyen and Stanton[18] also determined the rate constants for the OD + OD and OH + OD isotopic analogues. The theoretical rate constants for these isotopically substituted reactions were in reasonable agreement with the experimental measurements of Bedjanian et al.[10]

There are other theoretical investigations of reaction 1a but in the reverse direction.[23−26] These works were primarily interested in providing a theoretical description of the reaction of hypothermal O atoms with $H_2O$ that occurs in the upper atmosphere and the product state distribution of the resulting OH radicals. As such, the primary tool to extract rate constant and final state distributions information was classic trajectory calculations. Li and Guo[26] recently calculated a global HOOH($1^3A''$) PES at the CCSD(T)/AVTZ level of theory and used quasi-classical trajectory calculations to calculate forward and reverse rate constants for reaction 1a. This methodology does not account for tunneling and cannot describe reaction 1a at low temperatures where tunneling dominates the reactive flux.[17,18] Earlier work by Braunstein et al.[24] on the reverse reaction of 1a showed that both the $1^3A''$ and $2^3A'$ contributed to the reactive flux for $k_{-1a}$.

For the present experiments, a new reaction chamber was constructed that can span the temperature range 300−800 K. The probe laser was a tunable infrared laser system enabling OH to be detected on a single quantum state of the fundamental v(1,0) infrared transitions, thus, increasing the sensitivity of the OH concentration determinations by a factor of 15 over our previous measurements.

The OH radical was produced by laser flash photolysis of $N_2O$ to produce O($^1$D) atoms that reacted quickly with $H_2O$ to give OH radicals. The experiments were conducted at low pressures from 2 to 12 Torr depending on the temperature. The influence of collision broadening on the calculated absorption cross section was accounted for in the data analysis. The experiments were conducted in mixtures of $CF_4/N_2O/H_2O$ with an excess of $CF_4$.

## II. EXPERIMENTAL SECTION

The basic experiment and OH radical detection procedure used in this work was philosophically similar to our previous measurements[12] of $k_{1a}$. However, a new reaction chamber was constructed. This reaction chamber was designed to remove all possible wall effects and provide rapid removal of photolysis products by diffusion and flow. The chamber was constructed from a 304 stainless steel pipe, 48 in. long with a diameter of 6 in. The pipe was terminated by conflate stainless steel flanges. The photolysis and probe laser beams were admitted along the central axis of the pipe through 2 in. diameter UV grade $CaF_2$ Brewster angle windows mounted on stainless steel side arms 2 in. in diameter and nominally 4 in. long. The path length for a single pass of the probe laser through the photolysis zone was 151.5 cm. The windows were internally water cooled to suppress intensity fluctuations of the infrared laser radiation caused by refractive index variations from thermal gradients in the crystalline window material. The chamber was evacuated through 1 in. ports welded to each end flange offset 2.5 in. from the centerline. The gases were admitted through two concentric stainless steel tubes running the length of the chamber also offset by 2.5 in. from the centerline. The inner tube was 3/16 in. and the outer tube 3/8 in. in diameter. The outer tube was sealed at the opposite chamber wall and had fine 0.031 in. diameter holes space every 6 in. along its length. This arrangement provided rapid thermal equilibration and uniform


dx.doi.org/10.1021/jp409344q | J. Phys. Chem. A 2014, 118, 38−54

**Table 1. Reaction Mechanism Used To Model the OH Concentration Profiles**

| reaction | reactants | products | rate constant[a,b,c] | ref |
|---|---|---|---|---|
| 1a | OH + OH | $H_2O$ + O | measured | this work |
| 1b | OH + OH + $CF_4$ | $H_2O_2$ + $CF_4$ | $k_0 = 1.2 \times 10^{-30}(T/300)^{-3.2}$<br>$F_c = 0.43$<br>$k_\infty = 3.8 \times 10^{-11}(T/300)^{-0.5}$ | 15[d] |
| 1c | OH + OH + $N_2O$ | $H_2O_2$ + $N_2O$ | $k_0 = 9.5 \times 10^{-31}(T/300)^{-3.2}$<br>$F_c = 0.43$ | 15 |
| 1d | OH + OH + $H_2O$ | $H_2O_2$ + $H_2O$ | $k_0 = 4.6 \times 10^{-30}(T/300)^{-3.2}$<br>$F_c = 0.51$ | 15 |
| 2 | OH + O | $O_2$ + H | $1.12 \times 10^{-10} T^{-0.32} e^{177/T}$ | 35, 36 |
| 3a | OH + NO + $CF_4$ | HONO + $CF_4$ | $k_0 = 1.4 \times 10^{-30}(T/300)^{-2.6}$<br>$F_c = 0.81$<br>$k_\infty = 3.3 \times 10^{-11}(T/300)^{-0.3}$ | 39, 40 |
| 3b | OH + NO + $N_2O$ | HONO + $N_2O$ | $k_0 = 1.4 \times 10^{-30}(T/300)^{-2.6}$<br>$F_c = 0.81$ | 39, 40 |
| 3a | OH + NO + $H_2O$ | HONO + $H_2O$ | $k_0 = 7.0 \times 10^{-30}(T/300)^{-2.6}$<br>$F_c = 0.81$ | 39, 40 |
| 4a | OH + H + $CF_4$ | $H_2O$ + $CF_4$ | $k_0 = 3.7 \times 10^{-31}(T/300)^{-1.29}$<br>$F_c = 0.73$<br>$k_\infty = 1.9 \times 10^{-10}(T/300)^{-0.3}$ | 41 |
| 4b | OH + H + $N_2O$ | $H_2O$ + $N_2O$ | $k_0 = 3.7 \times 10^{-31}(T/300)^{-1.29}$<br>$F_c = 0.73$ | 41 |
| 4c | OH + H + $H_2O$ | $H_2O$ + $H_2O$ | $k_0 = 9.3 \times 10^{-31}(T/300)^{-1.29}$<br>$F_c = 0.73$ | 41 |
| 5 | OH + $H_2$ | $H_2O$ + H | $7.7 \times 10^{-12} e^{-2100/T}$ | 42 |
| 6 | OH + $H_2O_2$ | $H_2O$ + $HO_2$ | $2.90 \times 10^{-12} e^{-110/T}$ | 43 |
| 7 | O + $H_2O_2$ | OH + $HO_2$ | $1.1 \times 10^{-12} e^{-1990/T}$ | 44 |
| 8 | OH + $HO_2$ | $H_2O$ + $O_2$ | $4.8 \times 10^{-11} e^{250/T}$ | 45 |
| 9 | $HO_2$ + NO | $NO_2$ + OH | $3.0 \times 10^{-12} e^{290/T}$ | 46 |
| 10 | H + $HO_2$ | OH + OH | $8.0 \times 10^{-11}$ | 47 |
| 11a | $O(^1D)$ + $H_2O$ | 2OH | $1.88 \times 10^{-10}$ | 29 |
| 11b | | $O(^3P)$ + $H_2O$ | $1.9 \times 10^{-12}$ | 30 |
| 11c | | $H_2$ + $O_2$ | $<1.0 \times 10^{-12}$ | 30 |
| 12a | $O(^1D)$ + $N_2O$ | 2NO | $8.2 \times 10^{-11}$ | 31 |
| 12b | | $N_2$ + $O_2$ | $4.5 \times 10^{-11}$ | 32 |
| 12c | | $O(^3P)$ + $N_2O$ | $7.6 \times 10^{-12}$ | 32 |
| 13 | $O(^1D)$ + $CF_4$ | $O(^3P)$ + $CF_4$ | $2.0 \times 10^{-14}$ | 33 |
| 14 | X | X | $k_{diff}$(X) (diffusion) | 62 |

[a]Second-order rate constants, $k_i$ and $k_\infty$, units $cm^3$ $molecule^{-1}$ $s^{-1}$. [b]Third-order rate constants, $k_0$, units $cm^6$ $molecule^{-2}$ $s^{-1}$. [c]First-order rate constants, units $s^{-1}$. [d]See text for estimation of third body efficiencies

distribution of the admitted gases along the length of reaction chamber.

The main section of the chamber was heated by six 1000 W Watlow MI barrel heaters, 6 in. in diameter and 6 in. long, spaced about 2 in. apart. They were configured to operate in three separate heating zones: end, middle, and center. Each zone of two heaters was independently controlled by Watlow PM series PID temperature controllers. Only one thermocouple for each zone controlled the temperature setting for that zone. Also, the temperature of the chamber was monitored by a Watlow 1/8 in. diameter stainless steel sheath type K thermocouple. This thermocouple was placed inside a sealed 1/4 in. stainless steel tube open at one end and offset 2.5 in. from the chamber axis. This thermocouple could be positioned continuously along the chamber axis. Each side arm was heated by 3 ft. of high-temperature heater cable and controlled by a heat control unit. To reduce heat loss, the reaction chamber was wrapped with Cotronics 375 Thermal Stop ceramic tape and the side arms with Ultra-Temp ceramic tape. The temperatures at six equally spaced chamber locations, side arms and mounting flanges were distanced weighted and averaged to give the final reaction temperature. The temperature of one end zone was slightly higher than the other temperatures; for example, at 700 K, this temperature was 5 K higher than the other readings. The side arm temperatures were more difficult to regulate but were generally within ±5 K of the average temperature of the reaction chamber.

As in previous work,[12] the infrared laser beam was multipassed through the photolysis region using White cell optics; however, the White cell mirrors, UV−IR dichroic, and the protective ZnS Brewster-angle plate were external to the reaction chamber. This optical configuration caused the probe laser beam to be displaced horizontally and increased the difficulty in aligning the laser beam to the White cell axis. In the experiments, the optical path was varied from 1212 to 2424 cm. As the number of passes increased, the signal-to-noise ratio deceased because of increasing amplitude fluctuations of the probe laser intensity. This was particularly noticeable at the lowest ArF fluences, and in later experiments, the shortest path length was used exclusively.


dx.doi.org/10.1021/jp409344q | J. Phys. Chem. A 2014, 118, 38−54

The photolysis laser was a Lamda-Physik Compex 205 excimer laser operating at 193 nm. The laser repetition rate was varied from 1 to 5 Hz under various experimental conditions with no detectable change in the rate constant measurements; however, virtually all the data were collected at 2 Hz and with 200 laser-shot averaging. The infrared laser was a Linos Model OS 4500 OPO laser system modified to operate in a dual cavity mode. This provides a mode-hop free tuning range of over 0.25 $cm^{-1}$. The infrared laser was continuously monitored by a high-resolution (20 MHz) Bristol 621 IR wavemeter and a Burleigh model FCL-975 scanning etalon with a FSR of 7.5 GHz to ensure that the laser was operating on single axial mode.

The data acquisition hardware and software has been discussed previously.[27] The hardware was a National Instruments PXI based high-resolution digitizers and data acquisition modules controlled by a LabView program. Briefly, the infrared laser beam was split into two beams labeled I and $I_0$. The I beam passed through the photolysis zone and carried the absorption signal. Infrared polarizers were adjusted to keep the intensity of both beams equal. The signals from both beams were sampled using the dual inputs of a high-speed 16 bit A/D National Instruments PXI-5922 transient digitizer board. The two channels were subtracted in software to obtain the temporal absorption signal minus common-mode noise. The initial probe laser intensity was determined from the pretrigger value on the I channel. Both signals were also sent to two channels of a long memory 16 bit, 500 kHz, A/D digitizer subtracted and integrated for 20 ms. This signal was displayed on the computer screen in a single shot and a moving average strip-chart mode. These signals were used to tune and maintain the laser frequency on the peak of the OH spectral feature. The pulse-to-pulse variation of the ArF laser intensity was accounted for by monitoring the transmitted portion of the ArF radiation reflected off of the ZnS plate onto a Molectron J-50 power meter.

The gases used in the experiment were electronic grade $CF_4$, 99.999% pure, supplied by Linde and $N_2O$, 99.998% pure, supplied by AGA. The gas flows were monitored by in situ calibrated MKS Instruments mass-flow meters. The chamber pressure was measured by two Edwards model 600AB transducers covering different pressure ranges. Water vapor was admitted to the chamber through a double-trap bubbler system. The vapor pressure of the water was held constant using a Neslab RTE-111 bath recirculator. The nominal flow rates of the gases were $CF_4$, 300−400 sccm; $N_2O$, 80−150 sccm; and $H_2O$, 100−200 sccm. The operation of the water vapor injection procedure was checked at three different temperatures. The partial pressure of $H_2O$ was measured directly using infrared absorption spectroscopy on the $H_2O$ fundamental v(1,0,0) ← (0,0,0) ($5_{25}$ ← $6_{33}$) rotational transition at 3403.58 $cm^{-1}$. The line strength for this transition was taken from the Hitran[28] database, and peak absorption coefficients calculated. Without correcting for room temperature absorption, the spectroscopic measurements of the $H_2O$ concentration were within 10% of the calculated water vapor concentration indicating proper operation of the water injection system.

## III. RESULTS AND DISCUSSION

**A. Reaction Mechanism.** The reaction mechanism has been discussed in two recent articles.[12,13] The complete mechanism with updated rate constants, used in this work, is summarized in Table 1. However, the following four removal processes accounted for 98% of the removal flux of the OH radical. The OH radical was created by laser photolysis of $N_2O$ to produce $O(^1D)$ and the rapid reaction of $O(^1D)$ atoms with $H_2O$. Its subsequence removal by reaction and diffusion are as follows:

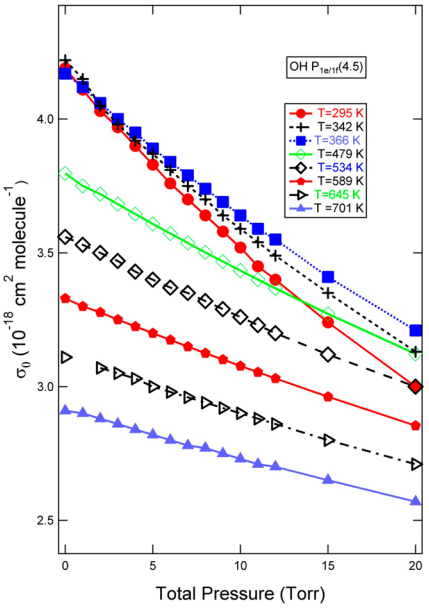


**Figure 1.** Line center absorption coefficient, $\sigma_0$, as a function of temperature and pressure. The maximum pressure used in the experiment was 12 Torr.

$$N_2O \xrightarrow{193\,nm} O(^1D) + N_2$$

$$O(^1D) + H_2O \rightarrow 2OH(v = 0,1,2) \qquad \Delta H^0 = -118.5\ kJ\ mol^{-1} \quad (11a)$$

$$OH + OH \rightarrow H_2O + O(^3P) \qquad \Delta H^0 = -67.2\ kJ\ mol^{-1} \quad (1a)$$

$$OH + OH + M \rightarrow H_2O_2 + M \qquad \Delta H^0 = -204.0\ kJ\ mol^{-1} \quad (1b,c,d)$$

$$OH + O(^3P) \rightarrow O_2 + H \qquad \Delta H^0 = -67.9\ kJ\ mol^{-1} \quad (2)$$

$$OH \rightarrow \text{diffusion} \quad (14)$$

At high initial OH concentrations and higher pressures, reactions 3 and 4 accounted for a few percent of the OH loss. The quenching of $O(^1D)$ by the three bath gases, reactions 11b, 12a and 13, produce reactive species that remove OH. However, recent work[29−33] has significantly reduced the uncertainty in the rate constants for these undesired side reactions, and they were accurately accounted for in the simulations of the OH temporal profiles. The fraction[34] of vibrationally excite OH radicals produced in reaction 11a is 0.33; however, it has been experimentally[12] shown that these states are quickly deactivated by the large concentration of $H_2O$ in the bath gas and do not influence the subsequent chemistry. Reaction 2 is the second most important chemical reaction removing the OH radical in the system. The rate constant[35,36] for reaction 2 is more than an order of magnitude larger than $k_{1a}$, and approximately, for every two OH radicals lost in reaction 1a another is lost due to reaction 2 so that the ratio of the reactive flux for these two processes is close to 0.5. The rate


dx.doi.org/10.1021/jp409344q | J. Phys. Chem. A 2014, 118, 38−54

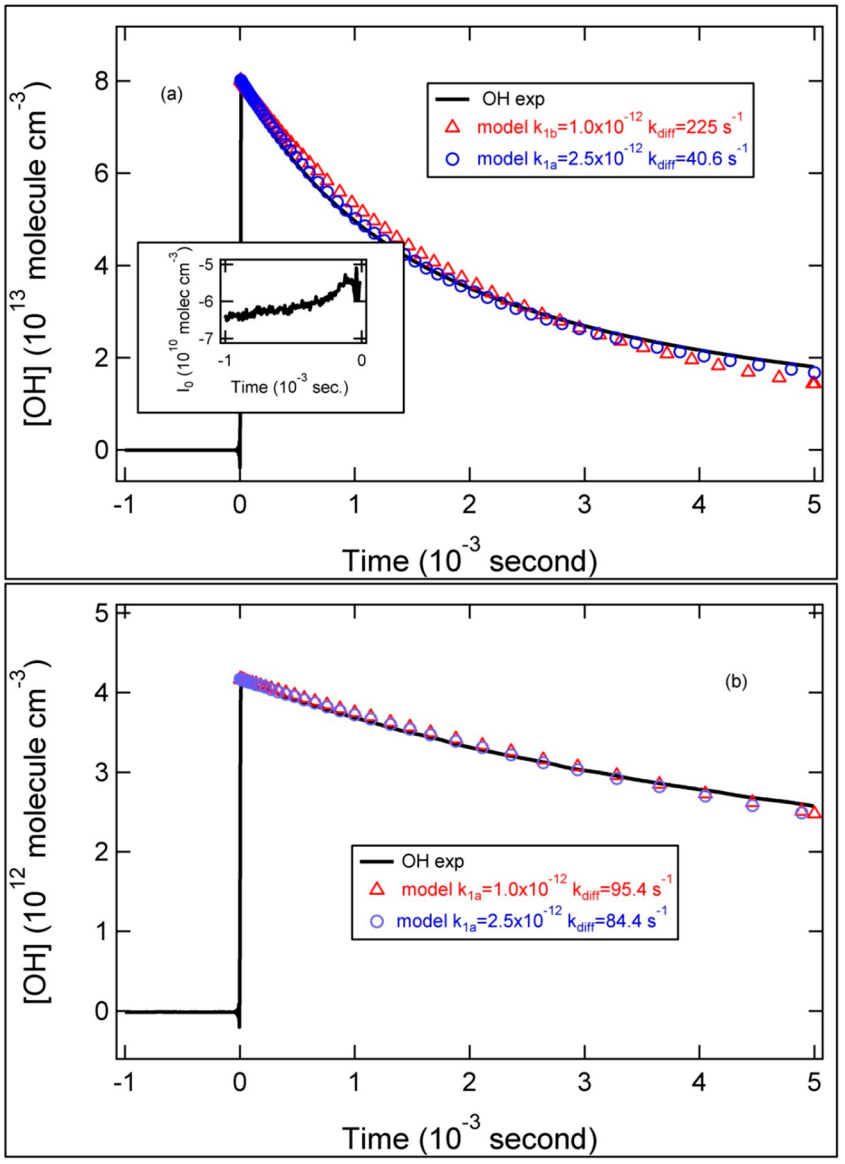


**Figure 2.** Determination of the optimum value of $k_{diff}$(OH) for a fixed value of $k_{1a}$. The solid black curve is the experimental profile. The inset shows an expanded view of the noise on the pretrigger baseline. At the peak the signal-to-noise is about $5 \times 10^3$. In Figure 2a, the red triangles show the best fit if $k_{1a} = 1.0 \times 10^{-12}$ cm$^3$ molecule$^{-1}$ s$^{-1}$, and in Figure 2b, the blue circles show the best fit for $k_{1a} = 2.5 \times 10^{-12}$ cm$^3$ molecule$^{-1}$ s$^{-1}$. As can be seen from the figures, the better fit is for $k_{1a} = 2.5 \times 10^{-12}$ cm$^3$ molecule$^{-1}$ s$^{-1}$ and $k_{diff}$(OH)=41 s$^{-1}$. The conditions of the experiment were $T$ = 479 K, $P_T$ = 12.05 Torr with partial pressures $P_{CF_4}$ = 6.18, $P_{N_2O}$ = 1.59, and $P_{H_2O}$ = 4.28 Torr.

constant, $k_2$, for reaction 2 was taken as measured by Robertson and Smith[35,35] over the temperature range 136−377 K and extrapolated to 700 K. Although there are other measurements in the literature, these measurements appear to be the most reliable and are in good agreement with the results of recent fully quantum time-independent calculations of Lique et al.[37]

The recombination rate constants in Table 1 were fit with the standard Troe parameters $k_0$ (low-pressure limit), $k_\infty$ (high-pressure limit), and $F_c$ (pressure broadening factor). The bimolecular rate constant, $k_f$, in the falloff region is represented by $k_f = k_\infty k_0[M]F/(k_0[M] + k_\infty)$, where $\log(F) = \log(F_c)/(1 + \{\log(k_0[M]/k_\infty)\}^2/N^2)$, with $N = 0.75 - 1.27\log(F_c)$. Generally, there are few data available on the relative collision efficiency of collision partners for recombination reactions involving two radicals. At the three lowest temperatures and highest pressures, reaction 1b accounted for up to 15% of the removal of OH. Troe[15] provides a detailed analysis of the available data for reaction 1b and provides collision efficiencies for seven different gases including $H_2O$ and $CO_2$. Altinay and Macdonald[38] studied the recombination reaction of $NH_2$ + $NH_2$ with a variety of collision partners including $CO_2$ and $CF_4$. Assuming $N_2O$ and $CO_2$ are about equally efficient as a collision partner for reaction 1b and the relative efficiencies of $CF_4$ and $CO_2$ are similar for OH recombination as $NH_2$ recombination, the relative efficiencies for $CF_4$:$N_2O$:$H_2O$ in reaction 1b are approximately 1.3:1.06:5.1, respectively. At 300 K, the values for He for $k_0$, $k_\infty$, and $F_c$ determined by Troe are in good agreement with those determined by Sellevåg et al.[16] using first-principle methods to describe the recombination reaction. The estimation of the collision efficiencies for the other two recombination reactions proceeded in a similar fashion. Water was assumed to be five more efficient than $N_2$, and the same relative efficiencies for $NH_2$ recombination was applied to $CF_4 \approx CO_2$ (as $N_2O$) and $N_2$. For reaction 3, the


dx.doi.org/10.1021/jp409344q | J. Phys. Chem. A 2014, 118, 38−54

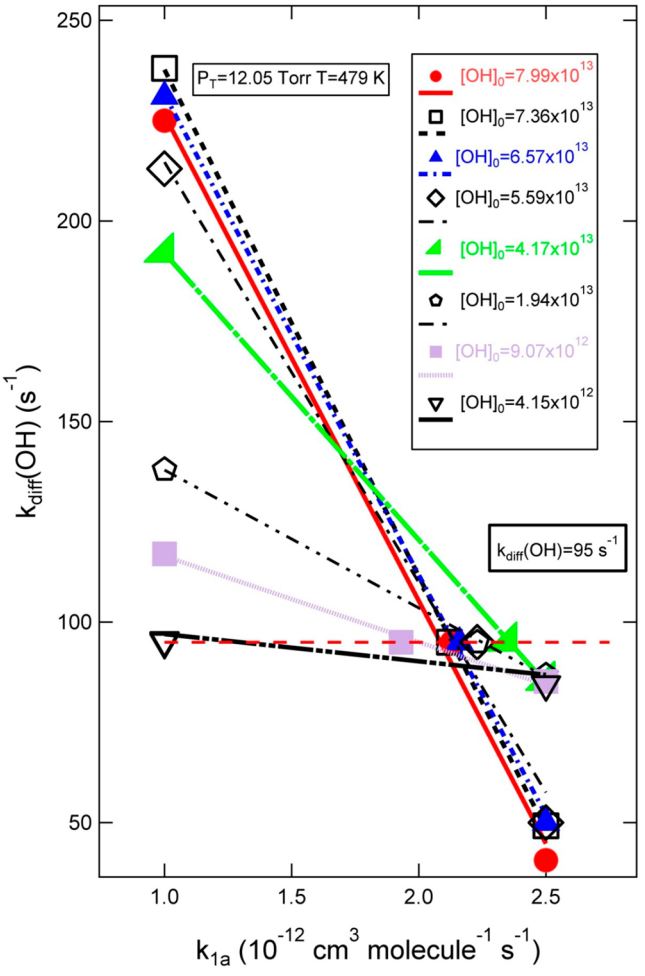


**Figure 3.** Results for the determination of the optimum values of $k_{diff}$(OH) for fixed values of $k_{1a}$, as shown in Figure 2, plotted for eight different initial OH concentrations. The results for $k_{diff}$(OH) given in Figure 2 are shown as the solid red circles and the solid red line. These plots are basically linear and only require two points to define a line. The value of $k_{diff}$(OH) that minimizes the scatter in $k_{1a}$ among the different initial OH concentrations provides the best $k_{diff}$(OH) for that set of experimental partial pressures. This value is illustrated by the long dashed red line for $k_{diff}$(OH) = 95 $s^{-1}$. Note that $k_{1a}$ cannot be smaller than 2.0 × $10^{-12}$ $cm^3$ $molecule^{-1}$ $s^{-1}$ because it is constrained by value of $k_{diff}$(OH) for small values of $[OH]_0$.

low-pressure measurements in $N_2$ of Atkinson and Smith[39] were used along with the data of Fulle et al.[40] for the high-pressure limiting rate constant and $F_c$. For reaction 4, the theoretical analysis of Sellevåg et al.[41] was used to provide the Troe parameters for a $N_2$ collision partner. The remaining rate constants were taken from the following sources.[42−47]

**B. Peak Absorption Cross Section OH($v$ = 1,0) $P_{1e/1f}$(4.5).** Absorption spectroscopy provides a direct measurement of a species concentration if both the path length, pl, and the absorption cross section, $\sigma(\nu)$, where $\nu$ is the transition wavenumber, are known. The Beer−Lambert Law relates the initial light intensity, $I_0$, and the transmitted light intensity, $I$, to the species concentration, [X], by $\ln(I_0/I) = pl\,\sigma(\nu)[X]$. The absorption cross section is given by the product of a line shape function, $g(\nu)$, and a line strength, $S$, $\sigma(\nu) = Sg(\nu)$. Over the last 15 years considerable progress has been made, both experimentally[48−51] and theoretically,[52−54] in the description of the dipole transition moments for the OH radical and the determination of appropriate line strengths. The early absorption experiments of Nelson et al.[48] combined with recent molecular-beam radiative-lifetime measurements[51] of OH($v$ = 1, $J$ = 3/2,$F_{1e/1f}$) levels have been combined with an extensive theoretical analysis by Van der Loo and Groenenboom[54,55] to yield very accurate and extensive information on the line strengths of the fundamental and overtone transitions in OH. The line strength for the OH(1,0) $P_{1e/1f}$(4.5) transitions was taken from this work. The temperature dependence of the line strength was determined using a rotational partition function calculated by a direct state count up to $J$ = 30.5 using the term values of Coxon[56] rather than the more recent values of Bernath and Colin.[57] The calculated line strengths were about 3% smaller than those given in the Hitran listings.[28]

At low pressure, $g(\nu)$ is given by a Doppler profile:

$$g(\nu) = \frac{\{\ln(2)/\pi\}^{1/2}}{b_D} \exp[-\ln(2)((\nu - \nu_0)/b_D)^2] \quad (1)$$

where $b_D$ is the Doppler HWHM given by $b_D$ = 3.582 × $10^{-7}\nu_0(T/M)^{1/2}$, where $\nu_0$ is the line center wavenumber and $T$ and $M$ have their usual meanings. The line center absorption cross section, $\sigma_0$, is given by $P'S$, where $P' = \{\ln(2)/\pi\}^{1/2}/b_D$. At modest pressures, the line shape function can be described[58] by a Voigt profile, a convolution between a Doppler and Lorentzian profiles, given by

$$g(\nu) = \frac{P'a}{\pi} \int_{-\infty}^{\infty} e^{-y2}/(a^2 + (\xi - y)^2)\, dy \quad (2)$$

where $a = b_L/b_D(\ln(2)^{1/2}$ and $\xi = (\ln(2))^{1/2}(\nu - \nu_0)/b_D$. The HWHM pressure broadening parameter, $b_L$, is given by $b_L^0P$, where $b_L^0$ is defined for a standard pressure and $P$ is the pressure of the collision partner. The area under an absorption feature is constant so that pressure broadening produces a decrease in the center line absorption cross section and an increase in the area in the wings of the absorption profile. To determine an accurate measurement of the OH radical concentration, collision broadening should be taken into account.

Schiffman and Nesbitt[59] have conducted a detailed study of pressure broadening and collision narrowing on the OH fundamental vibrational transition with several inert and diatomic molecules, He, Ar, $N_2$, and $O_2$. Such a detailed study is beyond the scope of this work, but a reasonable estimate of an appropriate pressure broadening parameter can be made. For bath gases used in the present work, $CF_4$, $N_2O$, and $H_2O$, there is little information available on collision broadening by these species with diatomic hydrides similar to OH, i.e., HF, DF, or HCl; however, this laboratory[38] has recently made estimates for the collision broadening by $CF_4$, $CO_2$, and $N_2$ on the $NH_3$ v(1,0,0,0) $^qQ_3(3)_{a/s}$ fundamental rotational transition with approximate efficiencies of 1:2:1, compared to $N_2$, which has a $b_L^0$ value[60] of 1.4 × $10^{-4}$ $cm^{-1}$ $Torr^{-1}$ at 295 K. Bonczyk[61] reported $b_L^0$ for the DF v(1,0) P(8) transition in collisions with $CF_4$ and $N_2$ of 5.9 × $10^{-5}$ and 7.1 × $10^{-5}$ $cm^{-1}$ $Torr^{-1}$ at 297 K. Schiffman and Nesbitt[59] measured $b_L^0$ for the OH v(1,0), $P_{1e/1f}$(4.5) lines of 7.58 × $10^{-5}$ $cm^{-1}$ $Torr^{-1}$ with $N_2$ as a collision partner. Undoubtedly, $b_L^0$ for $H_2O$ will be larger than that for $N_2$ in collisions with OH. The gas mixtures consisted of $CF_4$, $N_2O$, and $H_2O$ in various proportions, but generally, the partial pressures were in the ratio 3:1:1 for $CF_4$, $N_2O$, and $H_2O$, respectively. From the above data, it seems reasonable for the OH v(1,0) $P_{1e/f}$(4.5) transitions that $b_L^0(CF_4) \approx b_L^0(N_2)$, $b_L^0(N_2O) \approx 2b_L^0(N_2)$, and


dx.doi.org/10.1021/jp409344q | J. Phys. Chem. A 2014, 118, 38−54

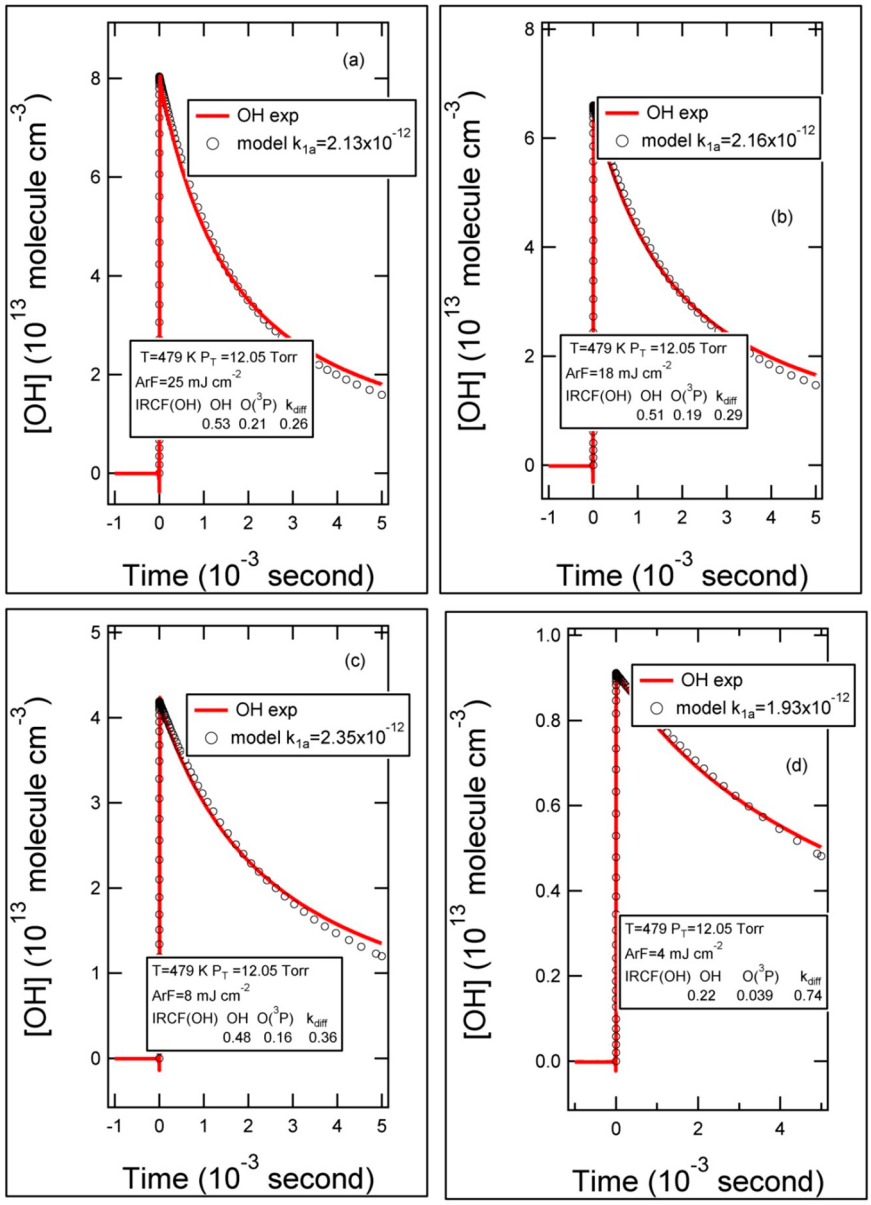


**Figure 4.** Typical OH temporal concentration profiles and the determination of $k_{1a}$ by computer simulations are shown for the experimental conditions given in Figure 2. The determination of $k_{diff}(OH) = 95\ s^{-1}$ for this experiment was shown in Figure 3. The four panels (a), (b), (c), and (d) were obtained at different ArF laser fluences, as indicated in each panel. The solid red curve is the experimental OH profile, and the open black circles are the computer simulation. The bottom legend contains the IRCF(OH) for removal of OH by reaction 1a, reaction 2, and diffusion.

$b_L^0(H_2O) \approx 3b_L^0(N_2)$. Using the generic composition ratio the effective $b_L^0$ for the mixture was estimated to be approximately $1 \times 10^{-4}$ at 295 K.

The temperature dependence of collision broadening parameters is complicated although classical theory suggests a $T^{-0.5}$ dependence. For OH, the Hitran[28] database gives the temperature dependence as $T^{-0.66}$, although there are no direct experimental measurements. This value was used in the present work. The calculated peak absorption cross section for the Λ-doublets of OH v(1,0) $P_{1e/f}(4.5)$ transition are shown in Figure 1 as a function of temperature and pressure.

**C. Determination of $k_{1a}$.** The major processes removing OH in the experiment are reactions 1a, 2, and 14. A procedure was developed to determine $k_{1a}$ and $k_{diff}(OH)$ for each set of initial conditions and is described below. In the present experiments, the peak absorption cross section on the fundamental OH vibrational transition at 295 K is about 15 times larger than that for the first overtone transition used in the previous[12] experiments and a larger range of OH concentrations was accessible in the present work. At high initial OH concentrations, $[OH]_0$, reaction 1a is responsible for removing more OH than reaction 14, $k_{diff}(OH)$, and conversely, at small initial OH concentrations diffusion dominates.

The initial OH concentration was varied eight times for a fixed set of initial conditions by changes in the photolysis laser intensity, through either the laser charging voltage or intensity attenuation by fine mesh stainless steel screens. For each OH profile, the initial $O(^1D)$ concentration created in the photolysis of $N_2O$ was found by varying the $O(^1D)$ concentration until the calculated initial OH concentration matched the experimental value to within ±0.5%. This ensures


dx.doi.org/10.1021/jp409344q | J. Phys. Chem. A 2014, 118, 38−54

Table 2. Summary of Experimental Conditions and Measurements for $k_{1a}$ 295 ± 2 K

| | partial pressure (Torr) | | | | | |
|---|---|---|---|---|---|---|
| pl[a] (cm) | $P_{CF_4}$ | $P_{N_2O}$ | $P_{H_2O}$ | $P_{total}$ (Torr) | range [OH][b] (×10$^{13}$) | $k_1$[c] (×10$^{-12}$) |
| *a* | 1.02 | 0.529 | 0.316 | 1.87 | 2.74−0.318 | 2.55 (±0.85)[d] |
| *a* | 0.989 | 0.298 | 0.721 | 2.01 | 2.62−0.313 | 2.27 (±0.28) |
| *b* | 1.59 | 0.537 | 0.891 | 3.02 | 2.31−0.295 | 2.56 (±0.42) |
| *a* | 1.50 | 0.453 | 1.09 | 3.04 | 4.23−0.505 | 2.37 (±0.44) |
| *b* | 2.05 | 0.414 | 0.608 | 3.07 | 2.23−0.213 | 2.49 (±0.040) |
| *a* | 1.96 | 1.02 | 0.612 | 3.59 | 5.97−0.663 | 2.62 (±0.48) |
| *b* | 2.03 | 0.685 | 1.26 | 3.98 | 3.18−0.320 | 2.61 (±0.58) |
| *a* | 2.20 | 1.15 | 0.68 | 4.02 | 6.26−0.722 | 2.50 (±0.68) |
| *a* | 2.06 | 0.710 | 1.08 | 4.05 | 6.69−0.768 | 2.43 (±0.34) |
| *a* | 2.68 | 0.541 | 0.863 | 4.08 | 2.79−0.277 | 2.34 (±0.69) |
| *b* | 2.71 | 0.584 | 0.805 | 4.10 | 2.93−0.368 | 2.29 (±0.54) |
| *a* | 2.65 | 1.37 | 0.818 | 4.84 | 8.58−1.00 | 2.62 (±0.79) |
| *b* | 2.60 | 0.875 | 1.59 | 5.07 | 3.86−0.433 | 2.69 (±0.31) |
| *a* | 2.84 | 0.900 | 1.34 | 5.08 | 7.99−0.983 | 2.59 (±0.46) |
| *b* | 2.88 | 0.776 | 1.65 | 5.31 | 3.65−0.402 | 2.31 (±0.27) |
| *a* | 3.50 | 0.705 | 1.12 | 5.33 | 3.40−0.393 | 2.37 (±0.38) |
| *a* | 1.66 | 3.33 | 0.531 | 5.52 | 1.70−0.200 | 1.96 (±0.57) |
| *b* | 3.24 | 0.840 | 1.85 | 5.93 | 4.11−0.456 | 2.29 (±0.34) |
| *a* | 3.36 | 1.06 | 1.58 | 6.00 | 7.87−0.962 | 2.59 (±0.27) |
| *b* | 3.08 | 1.04 | 1.89 | 6.01 | 4.51−0.512 | 2.62 (±0.24) |
| *a* | 3.36 | 1.73 | 1.04 | 6.13 | 9.99−1.10 | 2.73 (±0.71) |
| *a* | 4.02 | 0.812 | 1.31 | 6.14 | 3.98−0.477 | 2.41 (±0.42) |
| *a* | 4.49 | 0.907 | 1.44 | 6.84 | 4.35−0.465 | 2.45 (±0.21) |
| *a* | 3.98 | 1.20 | 1.83 | 7.01 | 8.85−1.03 | 2.53 (±0.44) |
| *b* | 3.61 | 1.22 | 2.21 | 7.04 | 4.86−0.470 | 2.83 (±0.21) |
| *b* | 4.70 | 0.952 | 1.51 | 7.16 | 4.68−0.517 | 2.51 (±0.33) |
| *a* | 5.16 | 1.04 | 1.66 | 7.86 | 4.72−0.551 | 2.61 (±0.27) |
| *a* | 4.53 | 1.37 | 2.10 | 8.00 | 9.39−1.16 | 2.62 (±0.34) |
| *b* | 4.07 | 1.38 | 2.56 | 8.01 | 5.42−0.578 | 2.79 (±0.40) |
| *a* | 4.39 | 2.27 | 1.36 | 8.02 | 10.9−1.26 | 3.00 (±0.35) |
| *a* | 5.62 | 1.14 | 1.63 | 8.39 | 5.15−0.628 | 2.63 (±0.26) |
| average | | | | | | 2.52 (±0.40) |

[a]pl is the path length: *a* = 2424 cm, *b* = 1818 cm, and *c* = 1212 cm. [b]Concentration units molecules cm$^{-3}$. [c]Rate constant units cm$^3$ molecule$^{-1}$ s$^{-1}$. [d]Average value of $k_{1a}$ for $[OH]_0 \geq 1.0 \times 10^{13}$ molecules cm$^{-3}$ with uncertainty $\pm 2\sigma$ in the scatter of the measurements.

that the initial concentrations of O($^3$P) and NO were accurately calculated in the computer simulations. The largest component of the gas mixture was $CF_4$. This gas was chosen to reduce the quenching of O($^1$D) to O($^3$P) and increase the mean molecular weight of the gas mixture and reduce diffusional losses.

The removal of OH by diffusion is a first-order process and is independent of OH concentration. The diffusion rate constant, $k_{diff}$(OH), is given by the product of a binary diffusion constant, $D_{12}$, and a geometrical factor, geom, describing the boundary conditions in the experiment, i.e., $k_{diff}(OH) = D_{12}\cdot$geom. The diffusion rate constant is inversely dependent on pressure. Decay by a first-order process is straightforward to implement in the kinetic model; however, the photolysis zone is a rectangle approximately 2 × 5 cm and the removal by diffusion is described by the sum of two exponential terms roughly corresponding to diffusion along the short and long axis of photolysis zone. These geometric constraints cannot be described by a single exponential decay in the kinetic model over the complete observation time. Instead, the OH profile was fit to a single exponential decay term for a fixed length of time so that the initial portion of the profile was adequately described. The binary diffusion constants for all species in the model were calculated by the diffusion volume method of Fuller at al.[62] and normalized to the measured $k_{diff}$(OH) to determine the geometrical factor for the other species. Over the temperature range of the experiments, the expected values for $k_{1a}$ range from 1.0 × 10$^{-12}$ to 2.5 × 10$^{-12}$ cm$^3$ molecule$^{-1}$ s$^{-1}$. For one set of partial pressures of the bath gases, each OH profile was fit to determine the optimum value of $k_{diff}$(OH) for two fixed values of $k_{1a}$, 1.0 × 10$^{-12}$ and 2.5 × 10$^{-12}$ cm$^3$ molecule$^{-1}$ s$^{-1}$. Two such profiles are shown in Figure 2 at a total pressure of 12.05 Torr and a temperature of 479 K. The experimental OH profiles are shown by the solid red lines and the calculated profiles by the open symbols. Note, the inset in Figure 2a shows the noise level on the pretrigger baseline. At the peak, the ac signal-to-noise was over 5000. It is clear the OH profiles were recorded with high signal-to-noise. It can be seen from Figure 2a that the $k_{1a}$ value of 2.5 × 10$^{-12}$ cm$^3$ molecule$^{-1}$ s$^{-1}$ is a superior fit the OH profile and the computed $\chi^2$ is almost an order of magnitude smaller than the fit for $k_{1a}$ equal to 1.0 × 10$^{-12}$ cm$^3$ molecule$^{-1}$ s$^{-1}$. It is important to note that a high signal-to-noise ratio is necessary to definitively discriminate between these pairs of fits. In Figure 2b, the opposite is true, both values of $k_{1a}$ provide nearly equally good fits, because $k_{diff}$(OH) accounts for over 90% of the OH removal flux. (The flux of a species, X, either removed or produced by a given process is termed an integrated reaction contribution factor, IRCF(X), and can be calculated from a


dx.doi.org/10.1021/jp409344q | J. Phys. Chem. A 2014, 118, 38−54

Table 3. Summary of Experimental Conditions and Measurements for $k_{1a}$ Measured from 342 to 701 K

| | | partial pressure (Torr) | | | | | |
|---|---|---|---|---|---|---|---|
| $T$ (K) | pl[a] | $P_{CF_4}$ | $P_{N_2O}$ | $P_{H_2O}$ | $P_{total}$ (Torr) | range [OH][b] ($\times 10^{13}$) | $k_1$[c] ($\times 10^{-12}$) |
| 342 ± 2 | c | 1.7 | 0.896 | 1.44 | 4.04 | 4.66−0.232 | 1.99 (±0.37)[d] |
| | | 2.19 | 1.09 | 1.73 | 5.01 | 5.87−0.284 | 2.17 (±0.40) |
| | | 2.02 | 1.55 | 1.45 | 5.03 | 6.23−0.280 | 2.02 (±0.23) |
| | | 2.60 | 1.32 | 2.10 | 6.02 | 6.73−0.318 | 2.08 (±0.073) |
| | | 2.42 | 1.86 | 1.74 | 6.02 | 6.92−0.331 | 2.15 (±0.24) |
| | | 3.53 | 1.86 | 1.64 | 7.03 | 6.78−0.340 | 2.09 (±0.16) |
| | | 3.03 | 1.55 | 2.48 | 7.06 | 7.38−0.360 | 2.17 (±0.19) |
| | | 4.22 | 1.83 | 1.98 | 8.03 | 7.21−0.360 | 2.18 (±0.15) |
| | | 4.01 | 1.66 | 3.34 | 9.01 | 7.99−0.381 | 2.28 (±0.14) |
| | | 4.83 | 1.95 | 2.25 | 9.04 | 7.56−0.388 | 2.20 (±0.07) |
| | | 4.45 | 1.84 | 3.71 | 10.0 | 8.38−0.401 | 2.37 (±0.08) |
| | | 5.52 | 1.90 | 2.61 | 10.0 | 7.71−0.374 | 2.31 (±0.09) |
| | | 6.16 | 1.86 | 2.99 | 11.0 | 7.97−0.421 | 2.40 (±0.17) |
| | | 4.86 | 1.99 | 4.21 | 11.1 | 8.12−0.411 | 2.48 (±0.05) |
| | | 5.86 | 1.71 | 4.34 | 12.0 | 8.02−0.370 | 2.54 (±0.19) |
| average | | | | | | | 2.23 (±0.33) |
| 368 ± 2 | b | 1.66 | 0.663 | 0.686 | 3.01 | 1.84−0.165 | 2.33 (±0.36) |
| | c | 1.84 | 0.723 | 1.22 | 3.78 | 4.01−0.206 | 1.97 (±0.37) |
| | b | 2.22 | 0.889 | 0.920 | 4.03 | 2.52−0.234 | 2.06 (±0.63) |
| | b | 2.74 | 1.10 | 1.12 | 4.97 | 3.53−0.256 | 2.03 (±0.47) |
| | c | 2.26 | 1.11 | 1.61 | 4.98 | 5.42−0.287 | 2.11 (±0.040) |
| | c | 2.50 | 1.27 | 1.26 | 5.03 | 3.79−0.195 | 1.91 (±0.65) |
| | b | 3.31 | 1.32 | 1.37 | 6.00 | 3.96−0.402 | 1.96 (±0.15) |
| | c | 2.71 | 1.33 | 1.97 | 6.01 | 6.27−0.318 | 2.16 (±0.33) |
| | c | 2.97 | 1.51 | 1.52 | 6.02 | 4.46−0.237 | 1.98 (±0.54) |
| | c | 3.16 | 1.56 | 2.29 | 7.00 | 6.82−0.363 | 2.12 (±0.14) |
| | b | 3.83 | 1.54 | 1.62 | 7.03 | 4.24−0.334 | 2.13 (±0.27) |
| | c | 3.43 | 1.75 | 1.82 | 7.04 | 4.86−0.268 | 2.06 (±0.74) |
| | b | 4.43 | 1.78 | 1.84 | 8.05 | 4.45−0.390 | 2.18 (±0.26) |
| | c | 3.95 | 2.02 | 2.10 | 8.06 | 5.52−0.287 | 2.04 (±0.37) |
| | c | 4.71 | 1.83 | 2.48 | 9.01 | 5.72−0.301 | 2.10 (±0.50) |
| | c | 4.21 | 1.77 | 3.06 | 9.04 | 7.70−0.390 | 2.34 (±0.27) |
| | c | 4.74 | 1.82 | 3.45 | 10.00 | 7.96−0.396 | 2.37 (±0.19) |
| | c | 5.30 | 1.85 | 2.86 | 10.0 | 5.97−0.336 | 2.13 (±0.28) |
| | c | 5.32 | 1.81 | 3.87 | 11.0 | 7.96−0.421 | 2.41 (±0.16) |
| | c | 5.93 | 1.93 | 3.2 | 11.1 | 6.15−0.346 | 2.20 (±0.22) |
| average | | | | | | | 2.13 (±0.28) |
| 479 ± 2 | b | 2.35 | 0.942 | 0.728 | 4.02 | 2.94−0.2801 | 1.70 (±0.76) |
| | c | 2.43 | 0.974 | 1.63 | 5.04 | 5.22−0.275 | 1.84 (±0.30) |
| | b | 2.96 | 1.19 | 0.878 | 5.05 | 4.04−0.329 | 1.81 (±0.16) |
| | c | 2.90 | 1.16 | 1.94 | 6.00 | 6.11−0.317 | 1.64 (±0.30) |
| | b | 3.52 | 1.41 | 1.09 | 6.01 | 4.40−0.385 | 1.75 (±0.14) |
| | c | 3.49 | 1.14 | 2.38 | 7.00 | 6.27−0.332 | 1.91 (±0.29) |
| | b | 4.13 | 1.66 | 1.28 | 7.07 | 4.79−0.474 | 1.78 (±0.13) |
| | b | 4.72 | 1.89 | 1.46 | 8.07 | 5.09−0.479 | 1.95 (±0.41) |
| | b | 5.74 | 1.48 | 1.79 | 9.00 | 4.90−0.388 | 1.90 (±0.24) |
| | c | 4.49 | 1.47 | 3.06 | 9.02 | 7.42−0.327 | 2.03 (±0.23) |
| | b | 5.26 | 2.11 | 1.64 | 9.06 | 5.42−0.226 | 1.85 (±0.25) |
| | c | 5.09 | 1.31 | 3.70 | 10.1 | 7.15−0.344 | 1.92 (±0.18) |
| | c | 5.55 | 1.67 | 3.78 | 11.0 | 8.05−0.415 | 2.15 (±0.22) |
| | c | 6.18 | 1.59 | 4.28 | 12.1 | 7.99−0.415 | 2.20 (±0.17) |
| average | | | | | | | 1.89 (±0.32) |
| 534 ± 3 | c | 1.82 | 1.16 | 1.03 | 4.01 | 4.12−0.201 | 1.67 (±0.31) |
| | b | 3.00 | 1.12 | 0.898 | 5.01 | 4.77−0.524 | 1.63 (±0.30) |
| | c | 2.26 | 1.53 | 1.22 | 5.01 | 5.83−0.275 | 1.75 (±0.46) |
| | b | 3.60 | 1.34 | 1.07 | 6.01 | 5.63−2.39 | 1.78 (±0.35) |
| | c | 2.71 | 1.83 | 1.47 | 6.01 | 6.45−0.383 | 1.93 (±0.38) |
| | b | 4.22 | 1.58 | 1.25 | 7.05 | 6.18−0.354 | 1.73 (±0.19) |
| | c | 3.15 | 2.14 | 1.75 | 7.05 | 7.09−0.285 | 1.99 (±0.22) |


dx.doi.org/10.1021/jp409344q | J. Phys. Chem. A 2014, 118, 38−54

**Table 3. continued**

| | | partial pressure (Torr) | | | | | |
|---|---|---|---|---|---|---|---|
| $T$ (K) | pl[a] | $P_{CF_4}$ | $P_{N_2O}$ | $P_{H_2O}$ | $P_{total}$ (Torr) | range [OH][b] ($\times 10^{13}$) | $k_1$[c] ($\times 10^{-12}$) |
| | *c* | 4.24 | 1.41 | 2.35 | 8.01 | 6.75−0.340 | 1.99 (±0.32) |
| | *b* | 4.80 | 1.80 | 1.41 | 8.02 | 6.57−0.298 | 1.87 (±0.29) |
| | *c* | 3.63 | 2.47 | 1.90 | 8.03 | 7.51−0.238 | 2.06 (±0.29) |
| | *c* | 5.24 | 1.37 | 2.35 | 8.97 | 7.07−0.315 | 2.03 (±0.22) |
| | *b* | 5.38 | 2.01 | 1.58 | 8.98 | 6.97−0.269 | 2.11 (±0.38) |
| average | | | | | | | 1.88 (±0.33) |
| 591 ± 3 | *c* | 2.04 | 1.07 | 0.912 | 4.02 | 4.53−0.140 | 2.15 (±0.52) |
| | | 1.85 | 1.25 | 0.963 | 4.06 | 4.20−0.169 | 1.89 (±0.40) |
| | | 2.31 | 1.54 | 1.19 | 5.04 | 5.28−0.297 | 1.79 (±0.22) |
| | | 2.70 | 1.12 | 1.36 | 5.18 | 5.49−0.244 | 1.90 (±0.21) |
| | | 2.72 | 1.82 | 1.42 | 5.96 | 6.02−0.278 | 2.21 (±0.25) |
| | | 3.16 | 1.31 | 1.60 | 6.07 | 6.38−0.298 | 2.04 (±0.39) |
| | | 3.63 | 1.51 | 1.86 | 7.01 | 7.30−0.327 | 2.25 (±0.41) |
| | | 3.21 | 2.14 | 1.67 | 7.02 | 6.65−0.346 | 2.14 (±0.14) |
| | | 4.39 | 1.36 | 2.27 | 8.03 | 7.54−0.279 | 2.25 (±0.23) |
| | | 3.67 | 2.46 | 1.92 | 8.05 | 7.28−0.404 | 2.26 (±0.16) |
| | | 4.90 | 1.76 | 2.42 | 9.07 | 8.00−0.348 | 2.21 (±0.26) |
| | | 4.18 | 2.83 | 2.06 | 9.08 | 7.71−0.503 | 2.19 (±0.12) |
| | | 5.64 | 1.52 | 2.85 | 10.0 | 8.10−0.330 | 2.22 (±0.28) |
| average | | | | | | | 2.12 (±0.32) |
| 645 ± 4 | *c* | 2.94 | 0.833 | 1.27 | 5.05 | 4.47−0.216 | 1.87 (±0.53) |
| | | 1.79 | 1.05 | 1.27 | 5.11 | 4.65−0.225 | 2.48 (±0.56) |
| | | 3.20 | 1.36 | 1.45 | 6.01 | 5.59−0.274 | 2.37 (±0.32) |
| | | 4.11 | 1.16 | 1.81 | 7.08 | 6.15−0.243 | 2.12 (±0.74) |
| | | 4.59 | 1.40 | 2.01 | 8.00 | 6.71−0.340 | 2.13 (±0.58) |
| | | 4.29 | 1.83 | 1.94 | 8.06 | 7.16−0.353 | 2.33(±0.36) |
| | | 5.28 | 1.49 | 2.28 | 9.05 | 7.38−0.369 | 2.19 (±0.50) |
| | | 5.10 | 1.63 | 2.36 | 9.09 | 7.04−0.371 | 2.20 (±0.20) |
| | | 5.85 | 1.66 | 2.51 | 10.0 | 7.92−0.737 | 2.12 (±0.36) |
| | | 5.47 | 2.07 | 2.51 | 10.0 | 8.06−0.390 | 2.42 (±0.46) |
| | | 6.38 | 1.81 | 2.82 | 11.0 | 8.42−0.530 | 2.13 (±0.43) |
| | | 6.17 | 1.98 | 2.86 | 11.0 | 8.08−0.364 | 2.18 (±0.30) |
| | | 6.72 | 2.15 | 3.11 | 12.0 | 8.69−0.421 | 2.38 (±0.21) |
| average | | | | | | | 2.22(±0.33) |
| 701 ± 5 | *c* | 3.22 | 1.43 | 1.35 | 6.01 | 7.76−0.263 | 1.64 (±0.69) |
| | | 3.93 | 1.99 | 1.08 | 7.00 | 4.40−0.240 | 1.93 (±0.78) |
| | | 3.76 | 1.68 | 1.59 | 7.03 | 5.46−0.274 | 1.81 (±0.93) |
| | | 4.51 | 2.25 | 1.24 | 8.00 | 5.06−0.279 | 1.88 (±0.73) |
| | | 4.28 | 1.91 | 1.84 | 8.03 | 5.78−0.330 | 1.78 (±0.70) |
| | | 5.26 | 2.25 | 1.48 | 9.00 | 5.59−0.296 | 1.80 (±0.59) |
| | | 4.93 | 1.92 | 2.15 | 9.01 | 6.20−0.366 | 1.76 (±0.56) |
| | | 5.32 | 2.02 | 2.67 | 10.0 | 6.76−0.365 | 1.99 (±0.64) |
| | | 5.90 | 2.51 | 1.68 | 10.1 | 5.96−0.345 | 2.07 (±0.80) |
| average | | | | | | | 1.85 (±0.26) |

[a]pl is the path length: $a$ = 2424 cm, $b$ = 1818 cm, and $c$ = 1212 cm. [b]Concentration units molecules cm$^{-3}$. [c]Rate constant units cm$^3$ molecule$^{-1}$ s$^{-1}$. [d]Average value of $k_{1a}$ for $[OH]_0 \geq 1.0 \times 10^{13}$ molecules cm$^{-3}$ with uncertainty $\pm 2\sigma$ in the scatter of the measurements.

kinetic model.) Figure 3 shows the plots of $k_{diff}$(OH) against $k_{1a}$ for all eight OH profiles under these experimental conditions. The best value of $k_{diff}$(OH) for this set of initial conditions was determined to be the value that provided the minimum scatter in the values of $k_{1a}$, indicated by the dashed red line at $k_{diff}$(OH) equal to 95 s$^{-1}$. All the OH profiles were then refit with $k_{diff}$(OH) equal to 95 s$^{-1}$ to determine the best value of $k_{1a}$ at each initial OH concentration.

Four OH profiles at different initial OH concentrations are shown in Figure 4 for this same experiment. Again the solid red lines are the experimental OH temporal profiles, and the open symbols are the calculated profile using the optimum values of $k_{1a}$ with $k_{diff}$(OH) equal to 95 s$^{-1}$. Note, the optimum profiles miss slightly near the end of the fit because the diffusion process in the model simulations is approximated by a single exponential decay, as discussed above. Furthermore, the determination of $k_{1a}$ is totally dominated by the initial portion of the profile whereas the later portion is dominated by diffusion, $k_{14}$. Also included in Figure 4 are the reaction path analysis, IRCF(OH), values for the dominant removal of OH. It is important to note that the fraction of OH loss by reaction 2 compared to reaction 1a decreases from 0.40 in Figure 4a to 0.18 in Figure 4d, but the optimum rate constants for $k_{1a}$ found in these two cases agree with each other well within the


dx.doi.org/10.1021/jp409344q | J. Phys. Chem. A 2014, 118, 38−54

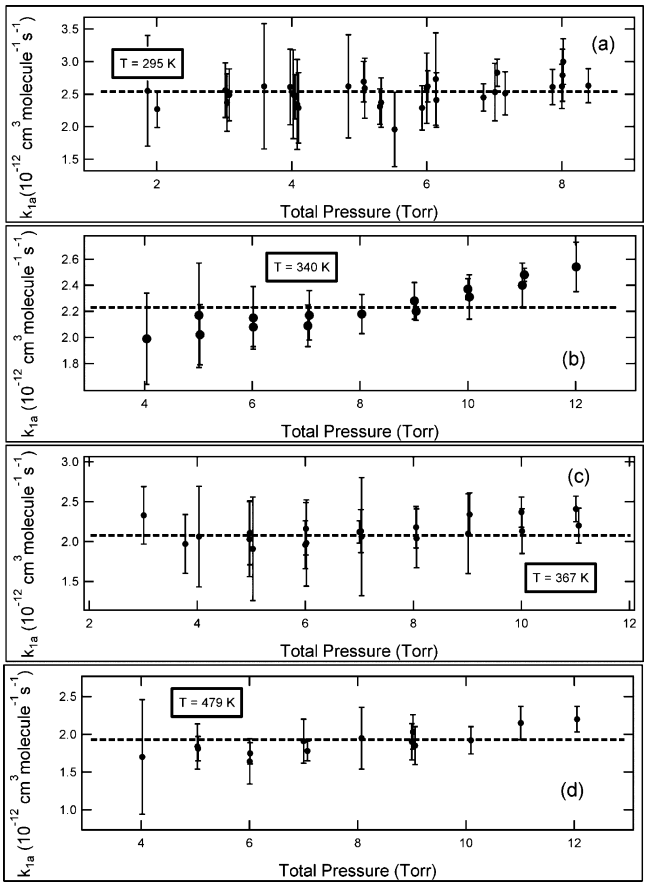


**Figure 5.** Summary of the experimental results for the determination of $k_{1a}$ as a function of total pressure. Each point is the average of at least six measurements at different initial OH concentrations as shown in Figure 4. The error bars are the $2\sigma$ limits in the experimental scatter. Only profiles with initial OH concentrations greater than $1.0 \times 10^{13}$ were included in the determination of $k_{1a}$. The results for (a) $T$ = 295 K, listed in Table 2, (b) $T$ = 340 K, listed in Table 3, (c) $T$ = 367 K, listed in Table 3, and (d) $T$ = 479 K, listed in Table 3.

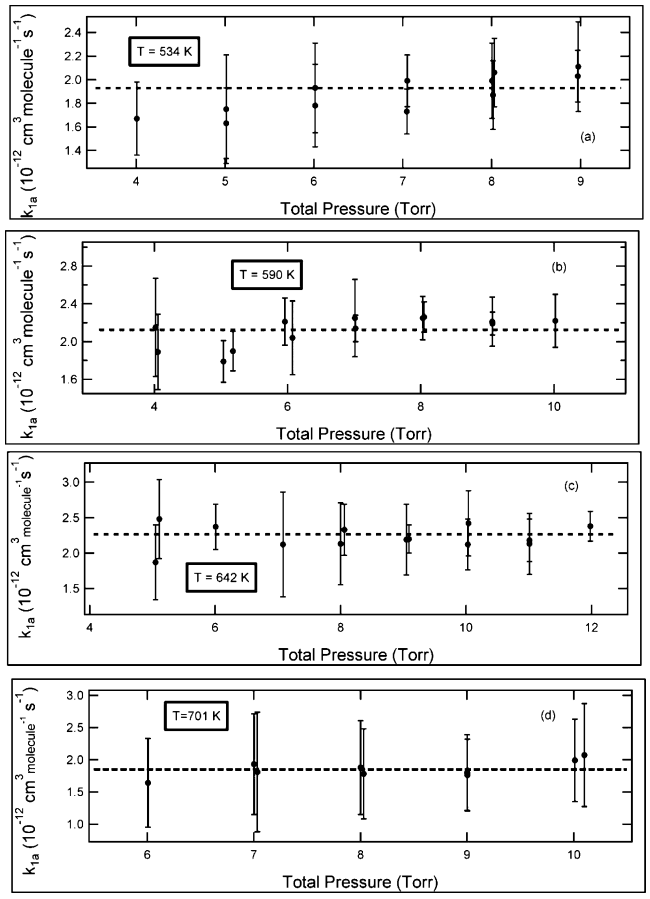


**Figure 6.** Same as Figure 5: (a) $T$ = 534 K; (b) $T$ = 590 K; (c) $T$ = 642 K; (d) $T$ = 701 K. All the data are summarized in Table 3.

goodness-of-fit parameters for these profiles and hence, independent of the value of $k_2$. The major loss processes for the O atoms are reaction 2 and diffusion. Although the O atoms were not monitored, their diffusion constant will be close to that of the OH radical, which was monitored, because of their nearly equal masses. The diffusional loss of O atoms accounted for the OH loss by reaction with O atoms decreasing as the initial OH concentration decreased. This suggests the value of $k_2$ used in the analysis must be close to the correct value.

Although no attempt was made to accurately quantify the photolysis laser fluence, an estimated prediction of the initial $O(^1D)$ concentration was made and compared to the predicted initial $O(^1D)$ concentration from the model in Table 1 based on the measured initial OH concentration as follows for the four separate measurements in Figure 4: (a) $7.7 \times 10^{13}$ and $5.0 \times 10^{13}$; (b) $5.7 \times 10^{13}$ and $4.1 \times 10^{13}$; (c) $4.4 \times 10^{13}$ and $3.5 \times 10^{13}$; (d) $1.3 \times 10^{13}$ and $1.2 \times 10^{13}$ in units molecules $cm^{-3}$ for photolysis estimation and model calculations of the initial $O(^1D)$ concentration, respectively. The photolysis estimated initial production of $O(^1D)$ is on average 22 ± 22% higher than calculated from the model in Table 1 based on reproducing the measured initial OH concentration by adjusting the $O(^1D)$ concentration, where the uncertainty is at the 95% level. Given the crude estimation of the laser photolysis beam energy (uncalibrated power meter) actually entering the reaction chamber and the rough estimate of the beam area (the beam divergence of the excimer laser is significant over the 151 cm optic path length), this is taken as reasonable agreement between the two measurements. If the photolysis beam width is increased from 2 to 2.5 cm, the average deviation between the two treatments is reduced to 6.2 ± 15%, reasonable agreement considering the rough estimate of the photolysis parameters. Of course, in the data analysis the variation of the initial $O(^1D)$ concentration to match the initial measurement of the OH concentration gives a much more reliable model prediction of the initial $O(^1D)$, $O(^3P)$, and NO concentrations. Of course there is no need for an elaborate treatment of the photolysis process because high-resolution laser absorption spectroscopy provides a direct measurement of the OH radical concentration. All of the OH profiles analyzed in this work were treated in the same fashion as outlined in the previous two paragraphs. The data are summarized in Table 2 for a temperature of 295 ± 2 K and for the other temperatures listed in Table 3. As the initial OH concentration decreases, the importance of $k_{1a}$ to the removal of OH also decreases and the uncertainty in the fit increases. Thus, only the experiments in which the OH concentration was greater than $1 \times 10^{13}$ molecules $cm^{-3}$ were used in calculating the average value of $k_{1a}$ for a given set of initial partial pressures. Usually, this resulted in the lowest two or three experiments not being included in the determination of the average of $k_{1a}$. In Table 3, the scatter in the temperature is the result of two or three experimental runs at the indicated average temperature. The determination of $k_{1a}$ as a function of


dx.doi.org/10.1021/jp409344q | J. Phys. Chem. A 2014, 118, 38−54

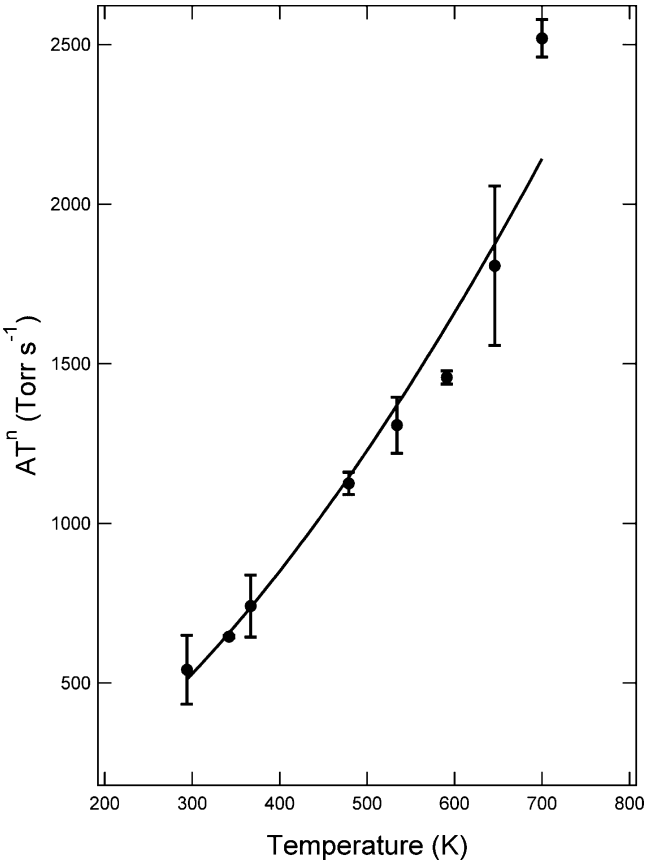


**Figure 7.** Determination of the temperature dependence of $k_{diff}$ (OH). The average of the slopes of the linear plots of $k_{diff}$(OH) as a function of $1/P$ at each temperature are plotted as a function of temperature. The error bars are the $2\sigma$ uncertainty in the scatter in the average slope at each temperature. As noted in the text, part of this scatter is due to geometrical changes in the optical alignment of the White cell mirrors and different gas compositions. The solid curve is a fit to the data of the form $AT^n$, where $A$ = 510 (Torr $s^{-1}$) and $n$ = 1.65.

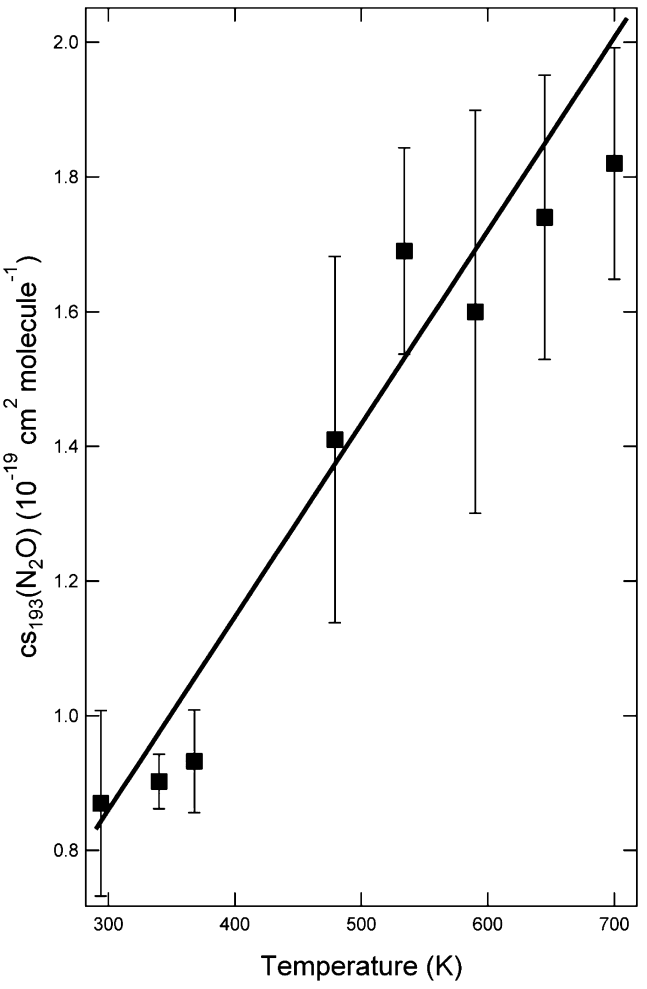


**Figure 8.** Temperature dependence of the 193 nm absorption coefficient of $N_2O$. Error bars are the $1\sigma$ uncertainty in the scatter. Only one measurement of $I_0$ was made for each experimental run. The solid line shows the accurate measurements of Sangwan et al.[13] These measurements show that the gas temperature has equilibrated to the chamber temperature.

temperature is summarized in Figures 5 and 6 as plots of $k_{1a}$ against total pressure. The error bars in each figure indicate the $\pm 2\sigma$ level in the scatter of the five or six measurements of $k_{1a}$ at a given set of experimental conditions. The short dashed line in each figure is the average value of $k_{1a}$ at the temperature of the experiment. As can be seen from Figure 1, collisional broadening reduces the peak absorption cross section of OH by up to 14% at 295 K as the pressure increases from 0 to 8 Torr. However, within the scatter of the measurements there is no systematic trend in the data as a function of pressure. As well, the importance of radical−radical recombination reactions, OH + OH, OH + NO, and OH + H (Table 1), all increase with increasing pressure, in particular $k_{1b/1c/1d}$ contributed up to 15% to the removal of OH at temperatures up to 366 K and the highest pressures. Again, there is no discernible trend in the data with increasing pressure, indicating that the recombination rate constants in Table 1 adequately described the chemistry.

The determination of $k_{diff}$(OH) in these experiments cannot be used to provide a measurement of the binary diffusion of the OH radical because of experimental variations in the gas composition, alignment of the White cell optics, and geometric constraints. However, it is possible to determine the temperature dependence of the diffusion rate constant for the OH radical expressed as

$$k_{diff}(\mathrm{OH}) = \frac{A}{P}T^n \qquad (3)$$

At each temperature, a plot of $k_{diff}$(OH) against $1/P$ gave a straight line of slope $AT^n$. The average values of these slopes for each temperature are shown in Figure 7 as the solid circles with error bars. The solid line is a fit to the data with $A$ equal to 510 $s^{-1}$ and $n$ equal to 1.65. The diffusion volume model of Fuller et al.[62] predicts a temperature dependence of $n$ equal to 1.75, in good agreement with the present measurements.

As discussed in the section II, the transmitted ArF laser radiation struck a ZnS plate after exiting the reaction chamber and was reflected onto a power meter. Nitrous oxide was the only species significantly contributing to the attenuation of the photolysis radiation. When the ArF laser intensity was recorded with an empty reaction chamber at the beginning of an experiment, a value of $I_0$ was established and the absorption coefficient for $N_2O$ could be calculated. The measurements were not intended to be accurate but only to indicate thermal equilibration of the gas mixture to the temperature of the


dx.doi.org/10.1021/jp409344q | J. Phys. Chem. A 2014, 118, 38−54

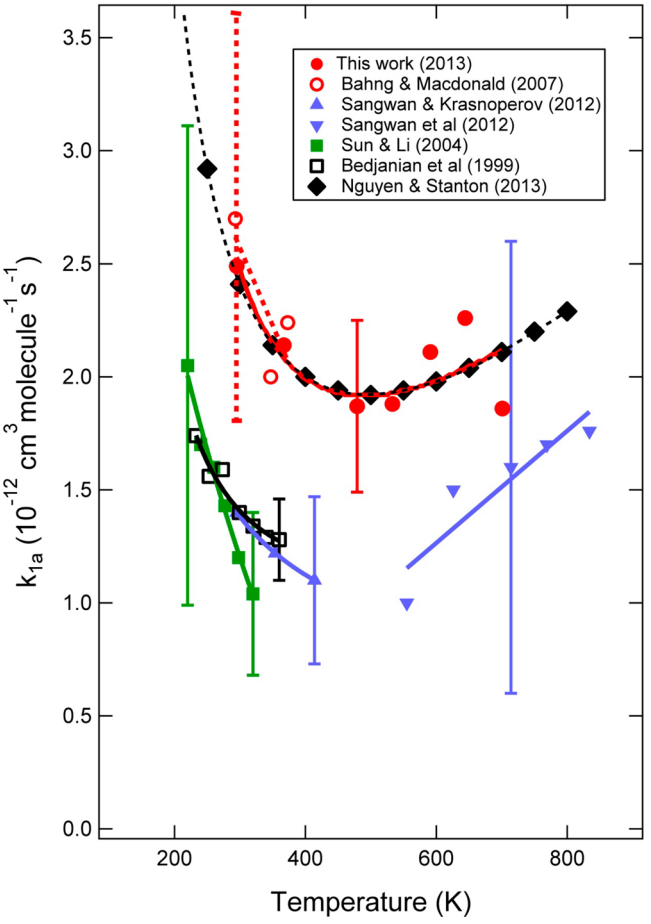


**Figure 9.** Summary of the temperature dependence of selected experimental and theoretical determinations of $k_{1a}$ for temperatures below 800 K is shown. The results of this work are given by the solid red circles. The solid red line is a fit to the data given by $k_{1a} = 4.79 \times 10^{-18} T^{1.79} \exp(879/T)$ cm$^3$ molecule$^{-1}$ s$^{-1}$. The other symbols are Bahng and Macdonald[12] (○), Sangwan et al.[13] (▼), Sangwan and Krasnoperov[14] (▲), Sun and Li[11] (■), Bedjanian et al.[10] (□), and Nguyen and Stanton[18] (◆). The associated lines are an aid for the eye. The error bars on the experimental measurements include both experimental scatter and systematic error at the $2\sigma$ confidence level. Note the excellent agreement between the direct measurements for $k_{1a}$ from this laboratory and the recent theoretical calculation of Nguyen and Stanton.[18]

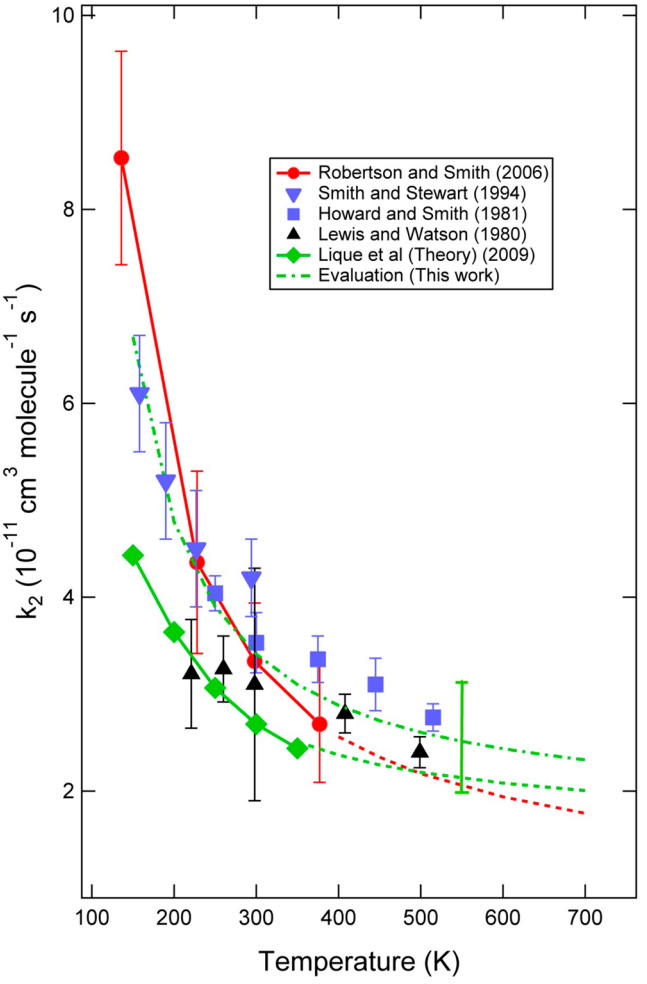


**Figure 10.** Summary of the available data on the temperature dependence of the rate constant for reaction 2, OH + O → H + $O_2$, over the temperature range 100−700 K. The measurements and predictions shown are as follows: Robertson and Smith[36] by the solid red circles and the extrapolation of the rate constant expression in Table 1 to 700 K by the dashed red line; Smith and Stewart[63] by the inverted blue triangles; Howard and Smith[64] by the blue squares; Lewis and Watson[65] by the black squares; Lique et al.[37] by the green diamonds and the extrapolation of the calculations to 700 K by the dashed green line; reevaluation of the temperature dependence of $k_2$ made in this work by the dot-dashed green line. The error bars are the given experimental uncertainties in the measurements at the 95% confidence level. The single error bar on the reevaluated fit represents the 95% confidence limit in the fitting procedure.

reaction chamber. The results of these measurements are shown in Figure 8 by the solid squares with error bars. The solid line gives the more accurate measurements of Sangwan et al.[13] As can be seen from Figure 8, the two measurements are in reasonable agreement.

Both the temperature dependence of $k_{diff}$(OH) shown in Figure 7 and the temperature dependence of the 193 nm $N_2O$ absorption cross section in Figure 8 clearly shows that the gas mixture had equilibrated to the chamber temperature.

**D. Comparison with Previous Work.** Figure 9 shows the comparison of the results of this work to selected previous experimental work[10−14] and a recent theoretical calculation[18] of $k_{1a}$ as a function of temperature. Not shown in Figure 9 are the experimental results for $k_{1a}$ from high-temperature shock tube studies[21−23] and the older theoretical calculations of Harding and Wagner.[17] There are six sets of experimental data included in this figure: the low-pressure discharge flow/mass spectrometry measurements of Bedjanian et al.[10] and Sun and Li,[11] the high pressure laser-flash photolysis and absorption spectroscopy measurements of Sangwan et al.[13] and Sangwan and Kransnoperov,[14] the laser-flash photolysis and the high-resolution laser absorption measurements of Bahng and Macdonald,[12] and the results of the present work. As noted in the Introduction, Nguyen and Stanton[18] used high level ab initio electronic structure calculations and semiclassical transition state theory to calculate $k_{1a}$. From Figure 9, it is clear that the experimental results from the present work are in excellent agreement with our previous measurements and the recent theoretical calculations. The scatter in the experimental data of the present work is reduced from our previous measurement because OH was detected on the fundamental transition with a larger peak absorption coefficient. The error bars on the experimental measurements in Figure 9 include


dx.doi.org/10.1021/jp409344q | J. Phys. Chem. A 2014, 118, 38−54

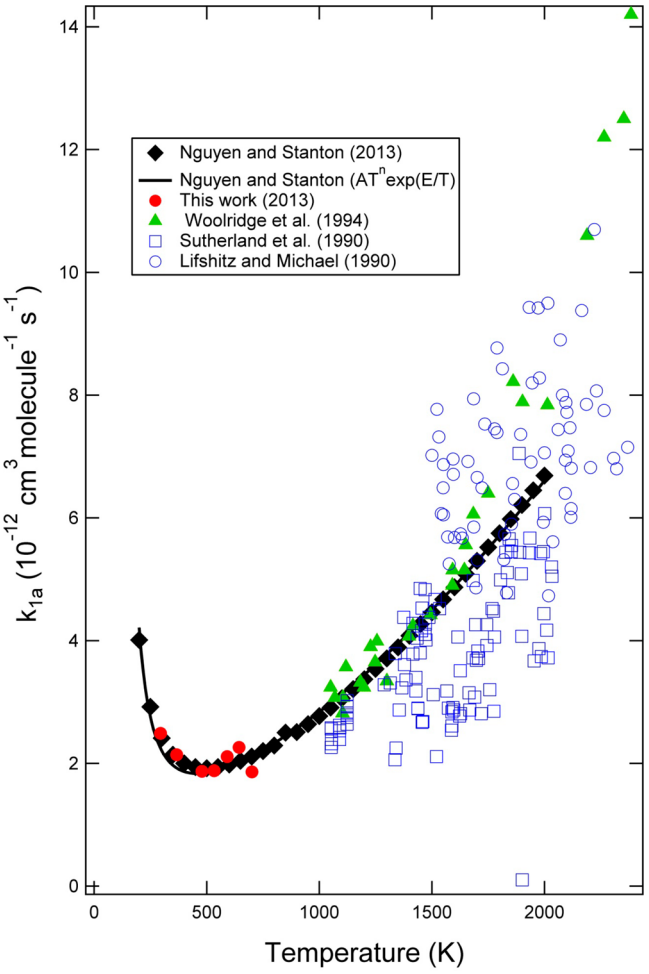


**Figure 11.** Fit to the theoretical calculations for the temperature dependence of $k_{1a}$ from 200 to 2000K along with high-temperature and the low-temperature measurements of this work. The symbols are as follows: $k_{1a}$ calculated by Nguyen and Stanton, black diamonds; the fit to the data gives $k_{1a} = 4.40 \times 10^{-16} T^{1.82} \exp(829/T)$ cm$^3$ molecule$^{-1}$ s$^{-1}$; this work, solid red circles; Woolridge et al., solid green triangles; Sutherland et al., open blue squares; Lifshitz and Michael, blue open circles. For clarity the experimental uncertainties are not shown.

both systematic and experimental uncertainty in the data at the $2\sigma$ confidence level.

The high-temperature measurements of $k_{1a}$, given by the blue tip down triangles from Sangwan et al.,[13] are in good agreement with both the present experimental measurements and theoretical values. The agreement improves with increasing temperature. The solid blue triangles show the recent low temperature measurements of Sangwan and Kransnoperov.[14] Although they have been corrected to the $2\sigma$ level-of-confidence in Figure 9, they just slightly overlap the present results. It should be pointed out that these experiments were not a direct measurement of $k_{1a}$. Instead, as a surrogate for monitoring the O atom product from reaction 1a, these workers used the O atom trapping reaction, $O(^3P) + O_2 + M \rightarrow O_3 + M$ and monitored the appearance of the $O_3$ product by UV absorption. Most of the experiments were conducted at pressures of 10 bar, producing short rise times for the $O_3$ signal with modest signal-to-noise. Interestingly, they modeled the rise in the $O_3$ signal with a kinetic mechanism but fixed the OH concentration profile to the observed one not the one generated by the simulation, preventing any feedback into the OH radical pool in the determination of $k_{1a}$. This rate constant should describe both the decay in the OH profile and the rise in the $O_3$ profile. The reported measurements of $k_{1a}$ were in good agreement with the results of Bedjanian et al.,[10] open black squares, and Sun and Li,[11] solid green squares.

As seen in Figure 9, the discharge flow/mass spectrometry measurements of Sun and Li[11] have a large uncertainty at the lowest temperature but improve with increasing temperature. The steep temperature dependence mirrors the rapid increase in the temperature dependence predicted by the theoretical calculations. In these experiments, the initial range of OH concentrations was limited to a factor of 2 and no first-order wall loss of OH radicals could be detected. In contrast, the measurements of Bedjanian et al.[10] have the lowest uncertainty in the $k_{1a}$ measurements and were conducted over a large range of initial OH concentrations. The measurements were also corrected for loss of OH on the reactor walls. Even so, the results of these measurements are outside the quoted uncertainty range of the present measurements and the theoretical calculations for $k_{1a}$. However, as discussed by Nguyen and Stranton,[18] Bedjanian et al. also measured the rate constant for all the isotopologues of reaction 1a over the same temperature range. These measurements were in reasonable agreement with the theoretical calculations of Nguyen and Stanton. As pointed out by Nguyen and Stanton, the higher values of $k_{1a}$ found in their work and reported by Bahng and Macdonald[12] were in good agreement with a purely statistical estimate for the mixed isotopic rate constant $k_{OH+OD}$ as the average of the two like isotopic rate constants, $0.5(k_{OH+OH} + k_{OD+OD})$. It is not clear why Bedjanian et al.'s measurements are not in better agreement with the experimental measurements of the present work and theory.

**E. Uncertainties in the Determination of $k_{1a}$.** In previous work,[12] it was shown that the decaying exponential distribution of OH radicals along the photolysis axis could influence the rate constant measurement if the transmitted photolysis intensity was lower than about 50%. An inspection of Tables 2 and 3 shows that, in general, only a few experiments were conducted in which the initial concentration of $N_2O$ was large enough to produce an absorbance larger than 0.6. In any case, no dependence on $N_2O$ concentrations on the determination of $k_{1a}$ was detectable and it was concluded that the axial radical distribution had little effect on the determination of $k_{1a}$.

The most important parameter in the determination of $k_{1a}$ is the concentration of the OH radical. There are three parameters that determine this concentration measurement by absorption spectroscopy: the line strength of the transition, the line profile, and the absorption path length. The interaction between line strength and collision broadening parameters has been discussed in section IIIA. The line strength of a OH $v(1,0)$ $P_{1e/f}(4.5))$ $\Lambda$-doublet was taken from the recent theoretical work of van der Loo and Groenenboom.[54] The theoretical calculations predicted a radiative lifetime of the OH($v$ = 1, $J$ = 3/2, $F_1$,e/f) states to be 58.3 ms, in excellent agreement with the experimental value of van der Meerakker et al.[51] These workers give an experimental uncertainty of ±3.4% in their measurement, assumed to be at the $1\sigma$ level-of-confidence. Various theoretical treatments from ref 54 give lifetimes slightly shorter by 0.75 ms than the experimental value but within 0.5% of each other and within 1% of the value calculated using the dipole moment function of Nelson et al.[50] Thus, the uncertainty in line strength is closer to that associated


dx.doi.org/10.1021/jp409344q | J. Phys. Chem. A 2014, 118, 38−54

with the theoretical treatment than that given by experiment and is taken as ±1%, at the 2$\sigma$ level. As discussed previously, the collision broadening parameters of OH by the gas mixture of $CF_4$, $N_2O$, and $H_2O$ was estimated to be $b_0 = 1.0 \times 10^{-4}$ $cm^{-1}$ $Torr^{-1}$, assuming an uncertainty of +50% in the collision broadening parameter; this results in a decrease of up to 7% in the line center OH absorption coefficient at the highest pressures and temperatures used in the experiments. This is the maximum influence at only three temperatures and half this value is taken as more representative of the contribution collision broadening makes to the complete data set. The corresponding increase in the OH radical concentration causes the optimum rate constant to decrease by roughly the same percentage and the contribution that collision broadening introduces to $k_{1a}$ was taken as 3.5%.

Reaction 2 and diffusion are the only two removal processes that contribute significantly to the OH decay besides reaction 1a. The recent measurements of Robertson and Smith were used in the data reduction as discussed in section IIIA; however, the highest temperature reached in both these experimental measurements and the recent theoretical calculations was 380 K, substantially lower than the maximum temperature reached in the present work. The long extrapolation of these results over the temperature range of the present work could introduce substantial error into the measurements of $k_{1a}$ at higher temperatures. Figure 10 shows the experimental measurements[36,63−65] and recent theoretical predictions[37] of the temperature dependence of $k_2$ from 100 to 700 K. Also included in Figure 10 is a reevaluation of $k_2$ by fitting all the temperature dependent data shown in the figure. The resulting rate expression is $k_2 = (1.7 \pm 0.56) \times 10^{-11}$ $\exp((202 \pm 40)/T)$ $cm^3$ $molecule^{-1}$ $s^{-1}$, where the uncertainties in the parameters are at the 95% confidence level. The evaluation of Atkinson et al.[66] was made before the measurements of Robertson and Smith[36] were available. As is evident from Figure 10, the temperature dependence of $k_2$ is small above 300 K; however, there is substantial uncertainty in the absolute value at higher temperatures, at the 95% confidence level. The extrapolated values of Robertson and Smith are in reasonable agreement with the measurements of Lewis and Watson[65] and the extrapolated theoretical predictions of Lique et al.[37] The experimental and systematic uncertainty in the measurement[36] of $k_2$ was given as 18% at the 2$\sigma$ level, but this does not overlap with the present extrapolation of the fit to complete data set from 100 to 500 K and should be increased to 24% to include this possibility. As discussed and shown in Figure 4, the measured $k_{1a}$ values were independent of the fraction of removal by reaction 2 and reaction 1a even though this decreased by a factor of 2 going from high (0.40) to low (0.17) initial OH concentrations, providing some confidence in the use of the rate expression for $k_2$ in Table 1. As shown previously,[12] the IRCF(OH) analysis can be used to estimate the maximum uncertainty in $k_{1a}$ caused by the uncertainty in $k_2$ to be ±12%, at the 95% confidence level.

It is difficult to easily quantify the contribution the uncertainty in $k_{diff}(OH)$ adds to the systematic error in $k_{1a}$ because of the wide variation in temperature, pressure and initial OH concentrations used to determine $k_{1a}$. As is evident from Figure 7, the scatter in the determination of the slope of the plots of $k_{diff}(OH)$ against $1/P$ could be large; however, some of this scatter was due to experimental variations and not due to the intrinsic uncertainty in determining $k_{diff}(OH)$. The uncertainty in determining the fit to data in Figure 7 was ±8.5% at the 1$\sigma$ level. This was taken to be a measure of the uncertainty in $k_{diff}(OH)$ for the complete data set at the 2$\sigma$ level-of-confidence because individual determinations of $k_{diff}(OH)$ were measured more accurately. An inspection of the legends in Figure 4 shows that the ratio of, $R$ = $IRCF_{diff}(OH)/ IRCF_{OH}(OH)$, varies from 0.46 to 3.36 from the highest initial OH concentration to the lowest. This variation is basically quadratic in the OH concentration because reaction removes two OH radicals. An estimate of the contribution the uncertainty the determination of $k_{diff}(OH)$ contributed to the uncertainty in $k_{1a}$ was taken with $R$ = 1 and was estimated to be ±8.5% at the 2$\sigma$ level.

In summary, the total systematic uncertainty in the determination of $k_{1a}$ comes from three sources: the uncertainty in determining the peak absorption coefficient of OH, 3.5%; the uncertainty in the rate constant for reaction 2, 12%; and the uncertainty in the determination of $k_{diff}(OH)$, 8.5%. Assuming these errors are uncorrelated, they can be combined with the average scatter in the experimental measurements of $k_{1a}$ of 15% to give a total error estimate, including experimental scatter and systematic errors of ±20% at the 95% confidence level.

**F. Extended Temperature Dependence of $k_{1a}$.** As is evident from Figure 10, there is excellent agreement between the experimental measurements from this laboratory and theoretical calculations of Nguyen and Stanton[18] from 300 to 700 K; however, the theoretical calculations cover the temperature range 200−2000 K. Figure 11 shows the comparison of the theoretical calculations with available high-temperature measurements[20−22] (200−2400) and the low-temperature measurements from this work (300−700 K). Woolridge et al.[20] measured $k_{1a}$ directly by laser-absorption spectroscopy whereas Lifshitz and Michael[21] and Sutherland et al.[22] used O atom atomic resonance absorption spectroscopy to measure the reverse reaction rate constant, $k_{-1a}$. The measurements of Sutherland et al. and Liftshitz and Michael have been converted to the forward rate constant using the thermodynamic data for OH from Ruscic et al.[67] A fit to the theoretical results over the temperature range 200−2000 K gives $k_{1a} = (4.43 \pm 1.48) \times 10^{-18} T^{(1.82\pm0.044)} \exp((829 \pm 25)/T)$ $cm^3$ $molecule^{-1}$ $s^{-1}$, where the uncertainty in the parameters is at the 95% level of confidence. As is evident from Figure 11, there is excellent agreement between the theoretical calculations of $k_{1a}$ and the experimental measurements of this work and the high-temperature measurements covering the temperature range 200−2000 K.

## IV. CONCLUSION

A new reaction chamber has been constructed to cover the temperature range from 295 to 800 K. At the highest temperatures, the temperature deviates less than ±3 K along its 151 cm length. The large diameter of the reaction chamber ensures that wall effects have a negligible effect on the kinetics. This new apparatus was used to study the OH + OH → $H_2O$ + O abstraction reaction on the $1^3A''$ PES over the temperature range 295−701 K. Over this temperature range, the value of $k_{1a}$ can be represented by $4.79 \times 10^{-18} T^{1.79} \exp(879/T)$ $cm^3$ $molecule^{-1}$ $s^{-1}$ with an uncertainty of ±20%, including experimental scatter and systematic errors at the 95% confidence limit. Although the new measurements were made in a totally different reaction chamber and used different spectroscopic transitions, they confirm the previous measurements of Bahng and Macdonald[12] and are in excellent


dx.doi.org/10.1021/jp409344q | J. Phys. Chem. A 2014, 118, 38−54

agreement with the recent theoretical calculations of Nguyen and Stanton.[18] (Figures 9 and 11) For reaction 1a, the previous measurements of Bedjanian et al.[10] are about 80% lower than the theoretical[18] calculations but for the other isotopic analogues their measurements are in reasonable agreement with the theoretical values. The present results do not agree with the recent low-temperature measurements (298−414 K) of Sangwan and Krasnoperov[14] but are in good agreement with the high-temperature measurements (555−834 K) of Sangwan et al.[13] over the overlapping temperature range.

The measurements from this laboratory provide a direct measurement of the rate constant for reaction 1a. The OH radical was detected on one of the Λ-doublets of the OH ($v$ = 1,0) $P_{1e/1f}(4.5)$ fundamental vibrational transition. The transition dipole moments of OH has recently been studied theoretically by van der Loo and Groenenboom,[54] and the line strengths for rotational transitions of the fundamental vibrational transition have been determined to within ±1% at the 95% confidence limit. The peak absorption coefficient for the probe transition was corrected for collision broadening.

As is evident from Figure 11, it may be concluded that the OH + OH abstraction reaction is well-characterized over a broad temperature range, 200−2000 K, from below room temperature to combustion temperatures.

## AUTHOR INFORMATION


### Corresponding Author

*R. G. Macdonald: e-mail, rgmacdonald@anl.gov.


### Notes

The authors declare no competing financial interest.

## ACKNOWLEDGMENTS

The authors thank Dr. S. Klippenstein and Dr. L. Harding of Argonne National Laboratory for valuable discussions on the OH + OH reaction. This work was performed under the auspices of the Office of Basic Energy Sciences, Division of Chemical Sciences, Geosciences, and Biosciences, U.S. Department of Energy under Contract Number DE-AC02-06CH11357.

## REFERENCES


(1) Burke, M. P.; Chaos, M.; Ju, Y.; Dryer, F. L.; Klippenstein, S. J. Comprehensive $H_2$ /$O_2$ Kinetic Model for High-Pressure Combustion. *Int. J. Chem. Kinet.* **2011**, *44*, 444−474.

(2) Takayanagi, T.; Kurosaki, Y.; Sato, K.; Misawa, K.; Kobayashi, Y.; Tsunashima, S. Kinetic Studies on the $N(^2D, ^2P)$ + $CH_4$ and $CD_4$ Reactions: The Role of Nonadiabatic Transitions on Thermal Rate Constants. *J. Phys. Chem. A* **1999**, *103*, 250−255.

(3) Dixon-Lewis, G.; Wilson, W. E.; Westenberg, A. A. Studies of Hydroxyl Radical Kinetics by Quantitative ESR. *J. Chem. Phys.* **1966**, *44*, 2877−2884.

(4) Breen, J. E.; Glass, G. P. Rate of Some Hydroxyl Reactions. *J. Chem. Phys.* **1970**, *52*, 1082−1086.

(5) Mulcahy, M. F. R.; Smith, R. H. Reactions of OH Radicals in the H-$NO_2$ and H-$NO_2$-CO Systems. *J. Chem. Phys.* **1971**, *54*, 5215−5221.

(6) Westenberg, A. A.; deHaas, N. Rate of the Reaction OH + OH → $H_2O$ + O. *J. Chem. Phys.* **1973**, *58*, 1066−4071.

(7) McKenzie, A.; Mulachy, M. F. R.; Steven, J. R. Kinetics of Decay of Hydroxyl Radicals at Low Pressure. *J. Chem. Phys.* **1973**, *59*, 3244−3254.

(8) Clynne, M. A. A.; Down, S. Kinetic Behavior of OH $X^2\Pi$ and $A^2\Sigma^+$ Using Molecular Resonance Fluorescence Spectroscopy. *J. Chem. Soc. Faraday Trans. II* **1974**, *70*, 253−266.

(9) Farquharson, G. K.; Smith, R. H. Rate Constants for the Gaseous Reactions OH + $C_2H_2$ and OH + OH. *Aust. J. Chem.* **1980**, *33*, 1425−1435.

(10) Bedjanian, Y.; Le Bras, G.; Poulet, G. Kinetic Study of OH + OH and OD + OD Reactions. *J. Phys. Chem. A* **1999**, *103*, 7017−7025.

(11) Sun, H.; Li, Z. Rate Constant Measurement for the OH + OH → $H_2O$ + O Reaction at 220−320 K Using Discharge Flow/Maas Spectrometer/Resonance Fluorescence Technique. *Chem. Phys. Lett.* **2004**, *399*, 33−38.

(12) Bahng, M.-K.; Macdonald, R. G. Determination of the Rate Constant for the $OH(^2\Pi)$ + $OH(^2\Pi)$ → $O(^3P)$ + $H_2O$ Reaction over the Temperature Range 293 − 373 K. *J. Phys. Chem A.* **2007**, *111*, 3850−3861.

(13) Sangwan, M.; Chesnokov, E. N.; Krasnoperov, L. N. Reaction OH + OH Studied over the 298−834 K Temperature and 1 − 100 bar Pressure Ranges. *J. Phys. Chem. A* **2012**, *116*, 6282−6294.

(14) Sangwan, M.; Krasnoperov, L. N. Disproportionation Channel of the Self-Reaction of Hydroxyl Radical, OH + OH → $H_2O$ + O, Studied by Time-Resolved Oxygen Atom Trapping. *J. Phys. Chem. A* **2012**, *116*, 11817−11822.

(15) Troe, J. The Thermal Dissociation/Recombination Reaction of Hydrogen Peroxide $H_2O_2$ ⇔ 2OH(+M) III. Analysis and Representation of the Temperature and Pressure Dependence over Wide Ranges. *Combust. Flame* **2010**, *158*, 594−601.

(16) Sellevåg, S. R.; Georgievskii, Y.; Miller, J. A. Kinetics of the Gas-Phase Recombination Reaction of Hydroxyl Radicals to Form Hydrogen Peroxide. *J. Phys. Chem. A* **2009**, *113*, 4457−4467.

(17) Harding, L. B.; Wagner, A. F. The Theoretical Study of the Reaction Rates of OH + OH ⇔ $H_2O$ + O. *22nd Symp. (Int.) Combust.* **1988**, 983−989.

(18) Nguyen, T. L.; Stanton, J. F. Ab Initio Thermal Rate Calculations of the HO + HO = $O(^3P)$ + $H_2O$ Reaction and Isotopologues. *J. Phys. Chem. A* **2013**, *117*, 2678−2686.

(19) Tajti, A.; Szalay, P. G.; Csaszar, A. G.; Kallay, M.; Gauss, J.; Valeev, E. F.; Flowers, B. A.; Vazquez, J.; Stanton, J. F. HEAT: High Accuracy Extrapolated Ab Initio Thermochemistry. *J. Chem. Phys.* **2004**, *121*, 11599−11613.

(20) Woolridge, M. S.; Hanson, R. K.; Bowman, C. T. A Shock Tube Study of the OH + OH → $H_2O$ + O Reaction. *Int. J. Chem. Kinet.* **1994**, *26*, 389−401.

(21) Lishitz, A.; Michael, J. V. Rate Constants for the Reaction O + $H_2O$ → OH + OH over the Temperature Range, 1500−2400 K, by the Flash-Photolysis Shock Tube Technique: A Further Consideration of the Back Reaction. *23th Symp. (Int.) Combust.* **1990**, 59−67.

(22) Sutherland, J. W.; Patterson, P. M.; Klem, R. B. Rate Constants for the Reaction O + $H_2O$ → OH + OH over the Temperature Range 1053−2033 K Using Two Direct Techniques. *23th Symp. (Int.) Combust.* **1990**, 51−57.

(23) Karkach, S. P.; Osherov, V. I. Ab Initio Analysis of the Transition States on the Lowest Triplet $H_2O_2$ Potential Surface. *J. Chem. Phys.* **1999**, *110*, 11918−9.

(24) Braunstein, M.; Panfilli, R.; Shroll, R.; Bernstein, L. Potential Surfaces and Dynamics of the $O(^3P)$ + $H_2O(X\ ^1A_1)$ → $OH(^2\Pi)$ + $OH(^2\Pi)$ Reaction. *J. Chem. Phys.* **2005**, *122*, 184307−13.

(25) Conforti, P. F.; Braunstein, M.; Braams, B. J.; Bowmwn, J. M. Global Potential Energy Surfaces for $O(^3P)$ + $H_2O(^1A_1)$ Collisions. *J. Chem. Phys.* **2010**, *133*, 164312−10.

(26) Li, J.; Guo, H. A New Ab Initio Global HOOH($1^3A''$) Potential Energy Surface for the $O(^3P)$ + $H_2O(X^1A_1)$ ↔ $OH(^2\Pi)$ + $OH(^2\Pi)$ Reaction. *J. Chem. Phys.* **2013**, *138*, 194304−10.

(27) Altinay, G.; Macdonald, R. G. Determination of the Rate Constant for the $NH_2(X^2B_1)$ + $NH_2(X^2B_1)$ Recombination Reaction with Collision Partners He, Ne, Ar, and $N_2$ at Low pressures and 296 K. Part 1. *J. Phys. Chem. A* **2012**, *116*, 1353−1367.

(28) Rothman, L. S.; Gordon, I. E.; Barbe, A.; Benner, D. C.; Bernath, P. E.; Birk, M.; Boudon, V.; Brown, L. R.; Campargue, A.; Champion, J. P.J.; et al. The HITRAN 2008 Molecular Spectroscopic Database. *J. Quant. Spectrosc. Radiat. Transfer* **2009**, *110*, 533−572.

(29) Dunlea, E. J.; Ravisankara, A. R. Measurement of the Rate Coefficient for the Reaction of $O(^1D)$ with $H_2O$ and Re-Evaluation of the Atmospheric OH Production Rate. *Phys. Chem. Chem. Phys.* **2004**, *6*, 3333−3340.
(30) Vranckx, S.; Peeters, J.; Carl, S. Kinetics of $O(^1D) + H_2O$ and $O(^1D) + H_2$: Absolute Rate Coefficients and $O(^3P)$ Yields between 227 and 453 K. *Phys. Chem. Chem. Phys.* **2010**, *12*, 9213−9221.
(31) Dunlea, E. J.; Ravishankara, A. R. Kinetic Studies of the Reactions of $O(^1D)$ with Several Atmospheric Molecules. *Phys. Chem. Chem. Phys.* **2004**, *6*, 2152−2161.
(32) Carl, S. A. A Highly Sensitive Method for Time-Resolved Detection of $O(^1D)$ Applied to Precise Determination of Absolute $O(^1D)$ Reaction Rate Constants and $O(^3P)$ Yields. *Phys. Chem. Chem. Phys.* **2005**, *7*, 4051−4053.
(33) Ravishankara, A. R.; Solomon, S.; Turnipseed, A. A.; Warren, R. F. Atmospheric Lifetimes of Long-Lived Halogenated Species. *Science* **1993**, *259*, 194−199.
(34) Tanaka, N.; Takayanagi, M.; Hanazaki, I. Nascent Rotational and Vibrational Distributions in $^{18}OH$ and $^{16}OH$ Produced in the Reaction $O(^1D) + H_2{}^{18}O$. *Chem. Phys. Lett.* **1996**, *254*, 40−46.
(35) Robertson, R.; Smith, G. P. Photolytic Measurement of the O + OH Rate Constant at 295 K. *Chem. Phys. Lett.* **2002**, *358*, 157−162.
(36) Robertson, R.; Smith, G. P. Temperature Dependence of O + OH at 136−377 K Using Ozone Photolysis. *J. Phys. Chem. A* **2006**, *110*, 6673−6679.
(37) Lique, F.; Jorfi, M.; Honvault, P.; Halvick, P.; Lin, S. Y.; Guo, H.; Xie, D. Q.; Dagdigian, P. J.; Klos, J.; Alexander, M. H. O + OH → $O_2$ + H: A Key Reaction for Interstellar Chemistry. New Theoretical Results and Comparison with Experiment. *J. Chem. Phys.* **2009**, *131*, 221104−4.
(38) Altinay, G.; Macdonald, R. G. Determination of the Rate Constant for the $NH_2(X^2B_1)$ + $NH_2(X^2B_1)$ and $NH_2(X^2B_1)$ + H Recombination Reactions with Collision Partners $CH_4$, $C_2H_6$, $CO_2$, $CF_4$, and $SF_6$ at Low Pressures and 296 K. Part 2. *J. Phys. Chem. A* **2012**, *116*, 2161−2176.
(39) Atkinson, D. B.; Smith, M. A. Radical-Molecule Kinetics in Pulsed Uniform Supersonic Flows: Termolecular Association of OH + NO between 90 and 220 K. *J. Phys. Chem.* **1994**, *98*, 5797−5800.
(40) Fulle, D.; Hamann, H. F.; Hippler, H.; Troe, J. Temperature and Pressure Dependence of the Addition Reactions of OH to NO and to $NO_2$. IV. Saturated Laser-Induced Fluorescence Measurements up to 1400 bar. *J. Chem. Phys.* **1998**, *108*, 5391−5397.
(41) Sellevåg, S. R.; Georgievskii, Y.; Miller, J. A. The Temperature and Pressure Dependence of the Reactions H + $O_2$ (+M) → $HO_2$ (+M) and H + OH (+M) → $H_2O$ (+M). *J. Phys. Chem. A* **2008**, *112*, 5085−5095.
(42) Orkin, V. L.; Kozlov, S. N.; Poskrebyshev, G. A.; Kurylo, M. J. Rate Constant for the Reaction of OH with $H_2$ between 200 and 480 K. *J. Phys. Chem.* **2006**, *110*, 6978−6985.
(43) Jiménez, E.; Gierczak, T.; Stark, H.; Burkholder, J. B. Ravishankara, Reactions of OH with $HO_2NO_2$ (Peroxynitric Acid): Rate Coefficients between 218 and 335 K and Product Yields at 298 K. *J. Phys. Chem. A* **2004**, *108*, 1139−1149.
(44) Wine, P. H.; Nicovich, J. M.; Thompson, R. J.; Ravishankara, A. R. Kinetics of $O(^3P_J)$ Reactions with $H_2O_2$ and $O_3$. *J. Phys. Chem.* **1983**, *87*, 3948−3954.
(45) Keyser, L. F. Kinetics of the Reaction OH + $HO_2$ → $H_2O$ + $O_2$. *J. Phys. Chem.* **1988**, *92*, 1193−1200.
(46) Seeley, J. V.; Meads, R. F.; Elrod, M. J.; Molina, M. J. Temperature and Pressure Dependence of the Rate Constant for the $HO_2$ + NO Reaction. *J. Phys. Chem.* **1996**, *100*, 4026−4031.
(47) Keyser, L. F. Absolute Rate Constant and Branching Fractions for the H + $HO_2$ Reaction fro 245 to 300 K. *J. Phys. Chem.* **1986**, *90*, 2994−3003.
(48) Nelson, D. D., Jr.; Schiffman, A.; Nesbitt, D. J.; Yaron, D. J. Absolute Infrared Transition Moments for Open Shell Diatomics from J Dependence of Transition Intensities: Application to OH. *J. Chem. Phys.* **1989**, *90*, 5443−5454.
(49) Nelson, D. D., Jr.; Schiffman, A.; Nesbitt, D. J. The Dipole Moment Function and Vibrational Transition Intensities of OH. *J. Chem. Phys.* **1989**, *90*, 5455−5465.
(50) Nelson, D. D., Jr.; Schiffman, A.; Nesbitt, D. J.; Orlando, J. J.; Burkholder, J. B. H + $O_3$ Fourier-Transform Infrared Emission and Laser Absorption Studies of OH($X\ ^2\Pi$) Radical: An Experimental Dipole Moment Function and State-to-State Einstein A Coefficients. *J. Chem. Phys.* **1990**, *93*, 7003−7019.
(51) van der Meerakker, S. Y. T.; Vanhaecke, N.; van der Loo, M. P. J.; Groenenboom, G. C.; Meijer, G. Direct Measurement of the Radiative Lifetime of Vibrationally Excited OH Radicals. *Phys. Rev. Lett.* **2005**, *95*, 013003−4.
(52) Langhoff, S. R.; Bauschlicher, C. W., Jr.; Taylor, P. R. Theoretical Study of the Dipole Moment Function of OH($X^2\Pi$). *J. Chem. Phys.* **1989**, *91*, 5953−5959.
(53) Holzclaw, K. W.; Person, J. C.; Green, B. D. Einstein Coefficients for Emission from High Rotational States of the OH($X\ ^2\Pi$) Radical. *J. Quant. Spectrosc. Radiat. Transfer* **1993**, *49*, 223−235.
(54) van der Loo, M. P. J.; Groenenboom, G. C. Theoretical Transition Probabilities for the OH Meinel System. *J. Chem. Phys.* **2007**, *126*, 114314−7.
(55) van der Loo, M. P. J.; Groenenboom, G. C. Erratum: "Theoretical Transition Probabilities for the OH Meinel System." *J. Chem. Phys.* **2008**, *128*, 159902-2.
(56) Coxon, J. A. Optimum Molecular Constants and Term Values for the $X\ ^2\Pi(v \leq 5)$ and $A\ ^2\Pi(v \leq 3)$. *Can J. Phys.* **1980**, *58*, 933−949.
(57) Bernath, P. F.; Colin, R. Revised Molecular Constants and Term Values for the $X^2\Pi$ and $B^2\Sigma^+$ States of OH. *J. Mol. Spectrosc.* **2009**, *257*, 20−23.
(58) Smith, M. A. H.; Rinsland, C. P.; Fridovich, B.; Rao, K. N. In *Molecular Spectroscopy: Modern Research*; Rao, K. N., Ed.; Academic Press: London, 1985; Vol. *III*, Chapter 3.
(59) Schiffman, A.; Nesbitt, D. J. Pressure Broadening and Collisional Narrowing in OH(v=1←0) Rovibrational Transitions with Ar, He, $O_2$, and $N_2$. *J. Chem. Phys.* **1994**, *100*, 2677−2689.
(60) Pine, A. S.; Markov, V. N. Self- and Foreign-Gas-Broadened Line Shapes in the $\nu_1$ Band of $NH_3$. *J. Mol. Spectrosc.* **2004**, *228*, 121−142.
(61) Bonczyk, P. A. Determination of the Linewidth Dependence on Foreign-Gas Pressure for 3.4-$\mu$m DF Spectra. *Phys. Rev. A* **1976**, *13*, 251−252.
(62) Fuller, E. N.; Ensley, K.; Giddings, J. C. Diffusion of Halogenated Hydrocarbons in Helium. The Effect of Structure on Collision Cross Sections. *J. Phys. Chem.* **1969**, *73*, 3679−3685.
(63) Smith, I. W. M.; Stewart, D. W. A. Low-temperature Kinetics of Reactions between Neutral Free Radicals Rate Constants for the Reactions of OH Radicals with N Atoms ($103 \leq T/K \leq 294$) and with O Atoms ($158 \leq T/K \leq 294$). *J. Chem. Soc., Faraday Trans.* **1994**, *90*, 3221−3227.
(64) Howard, M. J.; Smith, I. W. M. Direct Rate Measurements on the Reactions N + OH → NO +H and O + OH → $O_2$ + H from 250 to 515 K. *J. Chem. Soc., Faraday Trans. 2* **1981**, *77*, 997−1008.
(65) Lewis, R. S.; Watson, R. T. Temperature Dependence of the Reaction $O(^3P) + OH(^2\Pi) \rightarrow O_2 + H$. *J. Phys. Chem.* **1980**, *84*, 3495−3503.
(66) Atkinson, R.; Baulch, D. L.; Cox, R. A.; Crowley, J. N.; Hampson, R. F.; Hynes, R. G.; Jenkin, M. E.; Rossi, M. J.; Troe, J. Evaluated Kinetic and Photochemical Data for Atmospheric Chemistry. Volume I − Gas Phase Reactions of $O_x$, $HO_x$, $NO_x$ and $SO_x$. *J. Atmos. Chem. Phys.* **2004**, *4*, 1461−1738.
(67) Ruscic, B.; Boggs, J. E.; Burcat, A.; Császár, A. G.; Demaison, J.; Janoschek, R.; Martin, Jan M. L.; Morton, M. L.; Rossi, M. J.; Stanton, J. F.; et al. IUPAC Critical Evaluation of Therochemical Properties of Selected Radicals. Part 1. *J. Phys. Chem. Ref.* **2005**, *34*, 573−656.